POLITECNICO DI TORINO

Master's Degree in Physics of Complex Systems
(Percorso Nazionale)

Master's Degree Thesis

Time-sharing in Resource-Limited Biological Systems: An Exploration of Anti-phase Oscillations and Ribosome Competition

Supervisor	Candidate
Prof.ssa Carla BOSIA	Laura BATTAGLIA

December 2024

Summary

The aim of this thesis is to explore the possibility of observing *time-sharing* dynamics in a biological system characterized by a limited resource pool. The interest in this type of dynamics stems from the idea that competition for limited resources could promote temporal coordination strategies that optimize resource use, potentially benefiting protein synthesis and cell growth.

This research is based on the results of two scientific studies: "*Coupling between distant biofilms and emergence of nutrient time-sharing*" by Liu et al. [1] and "*Nonmodular oscillator and switch based on RNA decay drive regeneration of multimodal gene expression*" by Nordick et al. [2].

In the first article, it is observed that two *Bacillus subtilis* bacterial biofilms can coordinate their behavior through electrical signals and competition for glutamate, a limited resource. Under limited concentration of nutrient, biofilms alternate in their consumption of glutamate through a mechanism known as time-sharing, producing anti-phase oscillations that enable more efficient growth despite competition. This behavior suggests that temporal coordination in resource use may represent an adaptive advantage under conditions of limitation.

In the second article, a particular post-transcriptional model is analyzed. The model describes a set of reactions between mRNA and miRNA, resulting in sustained oscillations in their concentrations and in the concentrations of their complexes for specific sets of parameters. This model demonstrates that oscillation dynamics can emerge even in the absence of explicit feedback loops.

The central hypothesis of this thesis is that, by modifying the post-transcriptional model to include two independent systems sharing a single pool of ribosomes, it will be possible to observe dynamics similar to those of the biofilms, with the emergence of time-sharing. The analogy between ribosome competition and nutrient competition suggests that temporal coordination could also emerge in this context, optimizing protein synthesis efficiency.

Table of Contents

List of Tables

List of Figures

Chapter 1

Time-sharing in Biological Systems

Time-sharing, a strategy often used in resource management, involves the allocation of a limited resource in alternating intervals to different users, thus maximizing the efficiency of its use.

This thesis begins by investigating observations reported in the article "*Coupling between distant biofilms and emergence of nutrient time-sharing*" [1], which describes how two bacterial biofilms (*Bacillus subtilis*) competing for the same nutrient resource (glutamate) demonstrate time-sharing dynamics under nutrient-limiting conditions.

In this biological context, biofilms alternate their nutrient uptake, reducing direct competition and achieving increased growth efficiency through synchronized intervals of activity and dormancy.

Furthermore, the work by Park et al. "*Molecular Time Sharing through Dynamic Pulsing in Single Cells*" [3] describes similar dynamics at the molecular scale, where regulatory factors manage enzymatic competition through repetitive stochastic pulses, resulting in efficient time sharing of RNA polymerase (RNAP).

Inspired by these findings, this thesis aims to explore the dynamics of time-sharing in other biological contexts, examining whether similar principles can be applied across different scales of biological regulation. In this chapter we will analyze the two papers mentioned above and identify the common and pivotal characteristics necessary to have time-sharing of a limiting pool of resources.

1.1 Time-sharing at the population level: coupling between different biofilms

Bacterial communities can engage in complex interactions that coordinate collective behavior in response to environmental conditions. One such interaction is the coupling between biofilms, structured communities of bacteria embedded in a self-produced matrix, which optimizes resource utilization and improves growth efficiency under limiting conditions.

A striking example of this phenomenon is reported in the article "*Coupling between distant biofilms and the emergence of nutrient time sharing*" [1], which shows that two distant *Bacillus subtilis* biofilms can synchronize their metabolic activities through electrical signaling and competition for shared nutrients. The coupling between biofilms is mediated by potassium ion channels and shared nutrient demand. Initially, when the concentration of glutamate is high, this leads to in-phase metabolic oscillations.

However, as the concentration of glutamate is lowered, the biofilms switch from in-phase to anti-phase oscillations to resolve this competition. Stochastically, one of the biofilms will halt its growth. This allows the second biofilm to postpone halting its own growth, thus increasing the phase difference between the biofilms. This process destabilizes the in-phase dynamics, leading to anti-phase oscillations. This switch allows each biofilm to take turns consuming nutrients, effectively engaging in time-sharing. As a result, both biofilms achieve increased growth efficiency under reduced nutrient conditions. By alternating nutrient uptake, they avoid direct competition and optimize collective growth. This discovery underscores the ability of bacterial communities to extend interactions across spatially distant populations, coordinating to resolve conflicts and enhance survival—similar to resource allocation strategies in engineered systems.

1.1.1 Experimental Setup

The experimental setup involved growing two distant biofilms in a microfluidic chamber under controlled conditions. *Bacillus subtilis* biofilms were cultivated in a medium with a steady flow of essential nutrients, primarily glutamate as the nitrogen source. Time-lapse microscopy tracked the growth and metabolic oscillations of each biofilm, while electrical signaling was monitored using a fluorescent voltage indicator dye. Mathematical modeling complemented these observations, predicting how nutrient competition and electrical communication contribute to the dynamics.

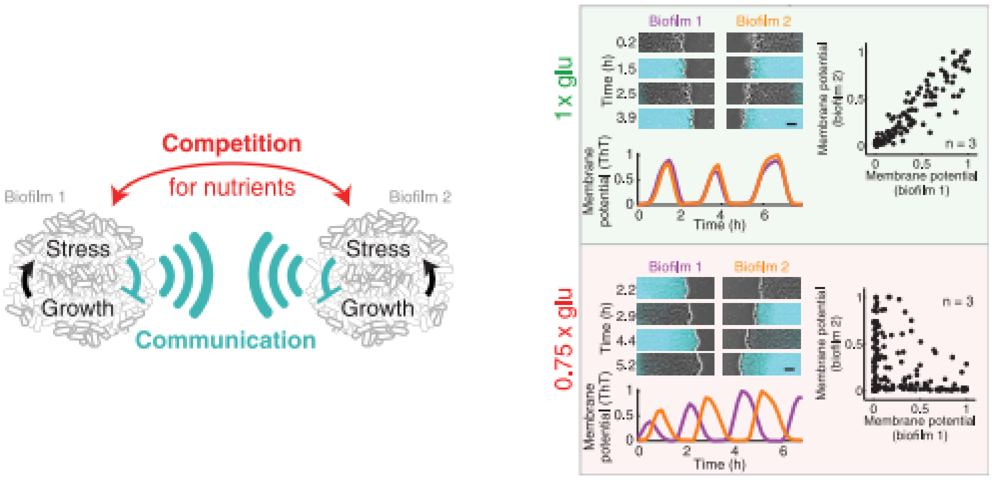

Figure 1.1: Figures adapted from [1]. Biofilm Coupling and Nutrient Time-Sharing. On the Left Panel: This schema illustrates the interaction between two distant biofilms through both electrical communication (cyan signals) and competition for nutrients (red arrows). On the Right Panel: Experimental results showing metabolic oscillations of biofilm pairs under different glutamate concentrations. At high glutamate concentrations (1x glu, top), biofilms exhibit in-phase oscillations (phase difference close to 0). At lower glutamate concentrations (0.75x glu, bottom), biofilms switch to antiphase oscillations (phase difference close to π). Each subpanel includes a filmstrip depicting membrane-potential oscillations in a representative biofilm pair (scale bars, 50 μm), corresponding time traces of membrane potential (color-coded for each biofilm), and scatterplots showing the membrane potential correlation of biofilm pairs across three experiments (one dot per time point).

1.1.2 Mathematical Model and Simulation Results

The results obtained in the work of [1] were based on direct laboratory observations. The authors conducted experimental studies to understand the dynamics of nutrient sharing between two biofilms and observed that these biofilms displayed distinctive oscillatory behavior in terms of nutrient uptake and growth rates. Following these observations, the authors employed mathematical modeling to validate the observed behavior, specifically using Kuramoto-like oscillators—mathematical models typically used to describe synchronization phenomena in coupled oscillatory systems—to describe the interaction between biofilms.

$$\begin{aligned}
\frac{d\theta_1}{dt} &= \omega_0 + \Delta\omega_1 + K\sin(\theta_2 - \theta_1) \\
\frac{d\theta_2}{dt} &= \omega_0 + \Delta\omega_2 + K\sin(\theta_1 - \theta_2) \\
\frac{dG}{dt} &= b - C_1 - C_2 - \delta_G(r_1 + r_2)G \\
\frac{dr_1}{dt} &= C_1 - \frac{\delta_r r_1}{k_r + r_1} \\
\frac{dr_2}{dt} &= C_2 - \frac{\delta_r r_2}{k_r + r_2}
\end{aligned} \tag{1.1}$$

where θ_1 and θ_2 represent the phases of biofilm oscillations, G is the concentration of available nutrients, r_1 and r_2 are the growth rates of the biofilms, and K, b, C_1, C_2, δ_G, δ_r, k_r, ω_0, and $\Delta\omega$ are system parameters, which have the following meanings:

- K represents the maximum coupling strength (related to communication efficiency between biofilms, which is modulated by glutamate concentration)

- b is the glutamate flow rate

- C_1 and C_2 are terms related to the glutamate consumption for biomass production, which saturate with increasing glutamate concentration

- δ_G represents the glutamate consumption rate for metabolic tasks

- δ_r is the biomass degradation rate

- k_r is the saturation threshold for biomass degradation

- ω_0 is the basal intrinsic frequency of biofilm oscillations

- $\Delta\omega$ represents the maximum glutamate-induced frequency shift, which reflects how nutrient stress impacts oscillation frequency

We reproduced the mathematical results presented in the article [1]. Figures 1.2 and 1.3 show the plots obtained during the simulations that faithfully reproduce those of the original article.

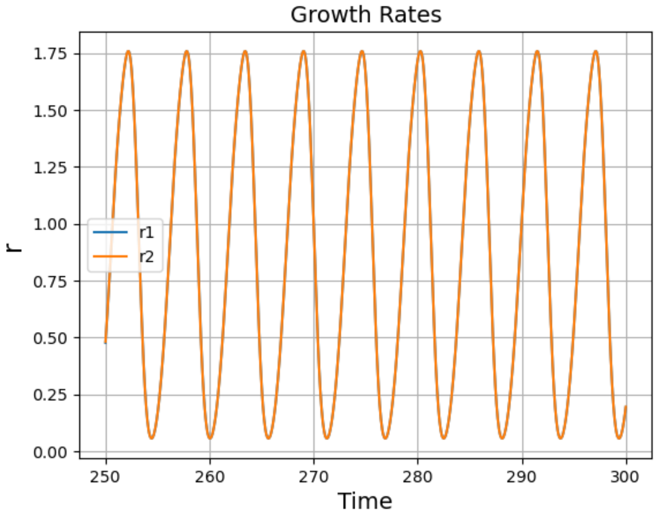

Figure 1.2: Growth rates r_1 and r_2 for Biofilm 1 and Biofilm 2 in in-phase dynamics. The curves were obtained by numerically integrating in Python the system of differential equations (1.1) under conditions of non-limiting glutamate availability, over a time span of 300 units, with results presented for the last 50 time units.

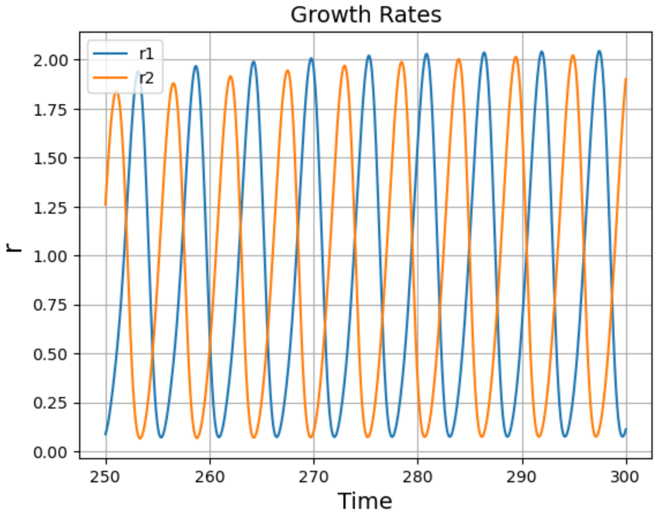

Figure 1.3: Growth rates r_1 and r_2 for Biofilm 1 and Biofilm 2 in anti-phase dynamics. The curves were obtained similarly to Figure 1.2, by numerically integrating the system of equations (1.1), but under conditions of limiting glutamate availability.

Moreover, the authors verified experimentally that anti-phase dynamics represent a gain for the two biofilms when there is a limited quantity of glutamate available. This anti-phase behavior allows for effective nutrient time-sharing, where each biofilm benefits from enhanced nutrient uptake efficiency during the off-phase of the other biofilm. The following figure provides a graphical and intuitive representation of the nutrient allocation process and the benefits for the two biofilms.

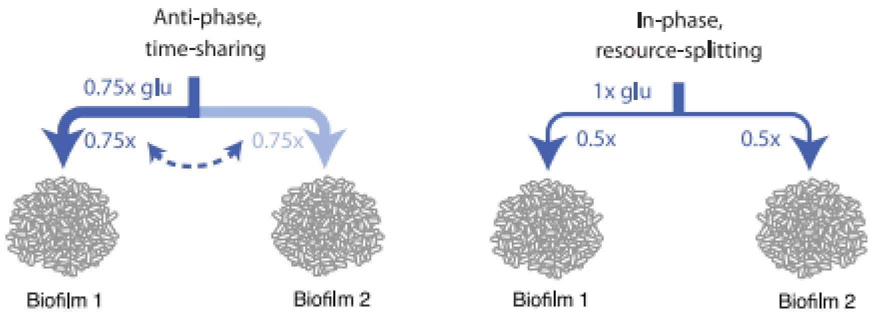

Figure 1.4: Figure adapted by [1]. Graphical representation of nutrient allocation and sharing between two biofilms. Antiphase oscillations (time-sharing) allow each biofilm to take turns accessing the full quantity of supplied nutrients during its growth phase. In contrast, in-phase oscillations (resource-splitting) only allow half of the supplied nutrients to each biofilm during its growth phase.

1.2 Time-sharing at molecular level in single cells: competition for RNA polymerase

The study “Molecular Time Sharing through Dynamic Pulsing in Single Cells” by Park et al. [3] provides another example that inspired this work, demonstrating that time-sharing dynamics can occur not only between biofilm communities but also within individual cells at molecular scales.

To better understand the study, it is first necessary to specify what RNA polymerase (RNAP) and sigma factors are, and what roles they play. The core RNA polymerase (RNAP) is an enzyme that synthesizes messenger RNA (mRNA) from a DNA template, which is a critical part of gene expression. In bacteria, RNAP needs sigma factors to recognize and bind to specific promoter regions of DNA, initiating transcription. In essence, RNAP is responsible for the conversion of genetic information into mRNA, which then serves as the blueprint for protein synthesis within the cell. Sigma factors are proteins that guide RNAP to specific sets of genes by binding to promoter regions on the DNA. There are multiple types of sigma factors, each of them controlling the expression of different genes, which often help cells adapt to changing conditions, such as nutrient scarcity or stress.

Sigma factors essentially act as the regulatory subunits of RNAP, determining which genes are transcribed under various environmental conditions.

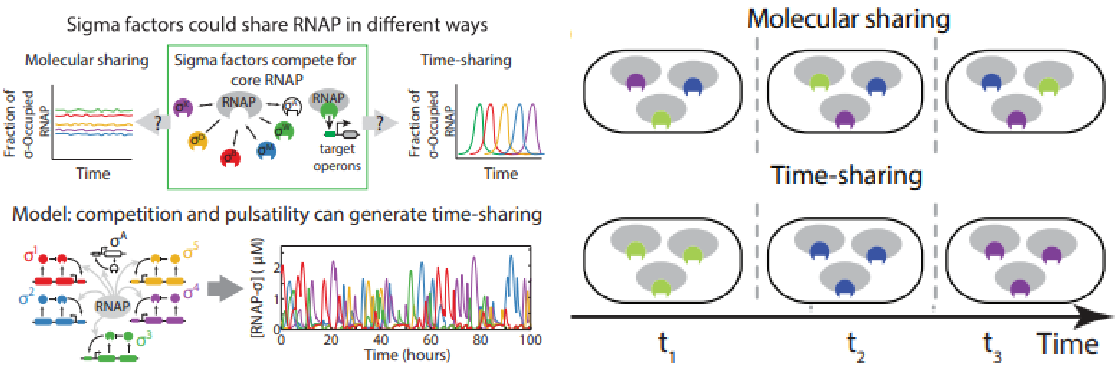

Figure 1.5: Figures adapted from [3]. Sigma factors compete for core RNAP, potentially leading to time-sharing dynamics. Left Panel: The top figure illustrates how sigma factors could share core RNAP through two modes: molecular sharing (left), where sigma factors utilize a constant fraction of RNAP over time, and time-sharing (right), where distinct sigma factors dominate RNAP use for specific time periods before transitioning to others. In principle, molecular sharing involves a stable partitioning of RNAP, while time-sharing creates dynamic changes with periods of dominant sigma factor activity, as shown in *Bacillus subtilis*. Only three sigma factor species are depicted for clarity. Right Panel: The figure further compares molecular sharing (where sigma factors coexist in each cell) and time-sharing (where individual sigma factors dominate in distinct intervals).

In the case studied in [3], different types of sigma factors in *Bacillus subtilis* compete for the core RNA polymerase (RNAP), present in limited amounts, through time-sharing dynamics. To effectively manage this competition, the sigma factors are activated in repetitive stochastic pulses, essentially taking turns in a coordinated manner. This pulsing behavior is a form of time-sharing that allows the cell to distribute the activity of RNAP across different gene sets over time, rather than trying to activate all at once. This strategy helps the cell optimize the use of RNAP while maintaining the flexibility to respond quickly to environmental signals—especially during times of energy stress.

Using time-lapse fluorescence microscopy, the authors observed the stochastic, repetitive activation of different sigma factors in real time at the single-cell level. This experimental approach allowed them to directly visualize the pulsatile behavior of sigma factors as they competed for the limited RNAP. By tagging each sigma factor with a specific fluorescent reporter, the researchers could monitor the activity of each factor over time, providing concrete evidence of the alternating pulses and their timings. These time-lapse experiments showed that different sigma factors rarely activated simultaneously, indicating a temporal separation that helps reduce competition for RNAP.

1.3 Discussion

Time-sharing appears to be a general principle across multiple levels of biological regulation, ranging from biofilm communities to individual cells at the intracellular level. These findings provide context for understanding how dynamic allocation of limited resources, such as glutamate or RNAP, might optimize biological functions—a central theme of this thesis. Moreover, the two studies discussed above highlight the key ingredients of time-sharing: (i) the presence of at least two "oscillators" coupled by a limiting shared resource, and (ii) the fact that their oscillations are out of phase, or in anti-phase, when the resource is scarse. In the following chapters, we will discuss how these ingredients can combine at the post-transcriptional level to allow for efficient time-sharing of a limited pool of ribosomes, the machineries necessary for protein translation. In this case, the two oscillators are represented by mRNAs, and the coupling resource is a fixed pool of ribosomes. By using mathematical modelling, we propose that, in order to efficiently use a few ribosomes, microRNAs induce mRNA oscillations through the presence of multiple binding sites on their targets. Before moving to our modelling strategy, in Chapter 3 we will briefly go over the different stages leading to gene expression with a focus on microRNA-mediated post-transcriptional regulation.

Chapter 2

Brief Summary in Gene Expression and Post-Transcriptional Regulation

One of the starting points of this thesis is the work *"Nonmodular oscillator and switch based on RNA decay drive regeneration of multimodal gene expression"* by Nordick et al. [2], which demonstrates the presence of oscillatory dynamics in the concentration of mRNA, microRNA (miRNA), and their complexes. Such findings highlight the intricate regulatory mechanisms that govern gene expression at the post-transcriptional level. Therefore, this chapter begins by reviewing key concepts related to gene expression and post-transcriptional regulation, focusing on the roles of miRNAs and ribosomes in regulating protein synthesis. This background is crucial for understanding the mechanisms that give rise to the oscillatory behaviors observed in mRNA-miRNA interactions, setting the foundation for the subsequent analysis in this thesis.

2.1 Gene Expression

Gene expression is a multi-step process that begins with DNA being transcribed into messenger RNA (mRNA), which is then translated into proteins [4]. The process involves RNA polymerase synthesizing an RNA strand from a DNA template, after which the mRNA is modified and transported for translation. During translation, ribosomes read the mRNA to assemble proteins from amino acids.

Regulatory mechanisms, including post-transcriptional regulation, are crucial for ensuring that proteins are synthesized in the right quantities, at the appropriate times, and in the correct locations. These regulatory processes influence mRNA stability, localization, and translation efficiency, often involving small RNA molecules like miRNAs.

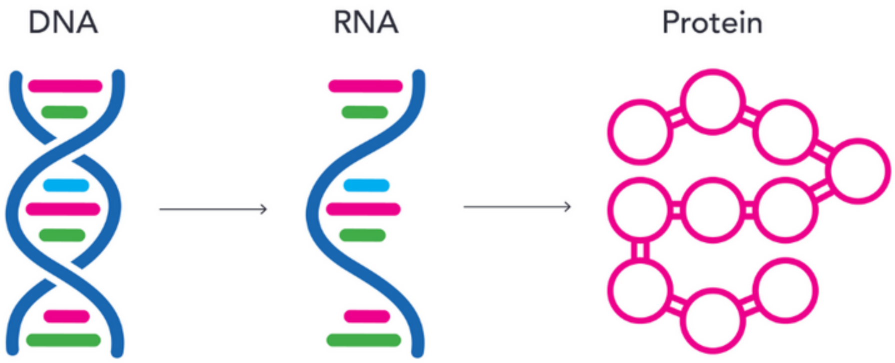

Figure 2.1: DNA to RNA to Protein Flowchart. Figure taken from *"Genomics 101: RNA vs DNA - What's the Difference"* by Genomics England.

2.2 Role of miRNAs

MiRNAs are small, non-coding RNA molecules, typically about 20-24 nucleotides long, that play a vital role in regulating gene expression after transcription has occurred. Unlike mRNAs, which carry the information needed to make proteins, miRNAs do not code for proteins themselves. Instead, they act as regulators by interacting with mRNAs to influence how much protein is made and when.

miRNAs work by binding to specific sequences in target mRNAs, usually in a region called the 3' untranslated region (3' UTR). This binding is often sequence-specific, meaning that miRNAs are complementary to the target mRNA sequence. Once a miRNA binds to its target mRNA, it can induce one of two outcomes: signaling either that the mRNA is degraded or preventing the mRNA from being translated by ribosomes into protein. In either case, the result is a decrease in the amount of protein produced from that mRNA [5].

This regulatory activity allows miRNAs to serve as "fine-tuners" of gene expression, ensuring that protein levels are carefully controlled in response to different developmental signals or environmental conditions. For instance, during embryonic development, cells need precise amounts of specific proteins at the right moments. miRNAs are essential for maintaining these exact levels, often by turning down the production of proteins that are no longer needed or whose overexpression could be harmful [6].

Another key role of miRNAs is in the cellular response to stress. In situations such as nutrient scarcity, disease, or environmental changes, miRNAs help the cell quickly adjust its protein production. By targeting mRNAs for degradation or preventing their translation, miRNAs allow the cell to conserve resources and ensure that only the most essential proteins are synthesized. This ability to modulate gene expression makes miRNAs vital players in maintaining cellular homeostasis [5].

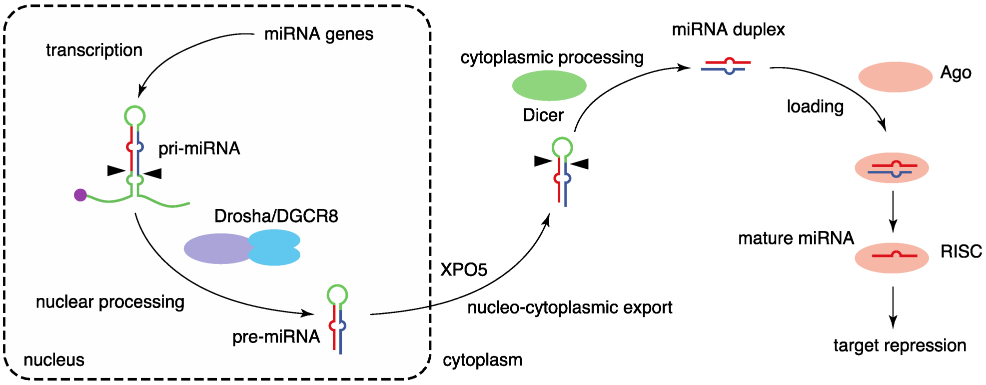

Figure 2.2: Figure taken from [7]. Overview of miRNA biogenesis, showing the steps from transcription of pri-miRNA in the nucleus, processing by Drosha/DGCR8 to pre-miRNA, export to the cytoplasm, and further processing by Dicer into a mature miRNA duplex. The mature miRNA is then loaded into the RNA-induced silencing complex (RISC) to regulate gene expression.

2.3 Role of Ribosomes in Translation

Ribosomes are molecular machines responsible for translating mRNA sequences into functional proteins. They are composed of ribosomal RNA (rRNA) and proteins, forming two subunits that come together during translation [8]. Ribosomes move along an mRNA strand, reading its codons and recruiting corresponding transfer RNAs (tRNAs) to assemble amino acids in the correct sequence to form a polypeptide chain. In this way, ribosomes are essential for the final step of gene expression, as they convert the genetic code into the structural and functional molecules of the cell.

Ribosomes play a key role in gene regulation, particularly concerning resource allocation within the cell. Since the number of ribosomes in a cell is finite, their availability can directly influence translation efficiency, especially during times of increased demand or stress [9]. The availability of ribosomes becomes an important regulatory point when multiple mRNAs compete for translation, affecting how efficiently proteins are synthesized.

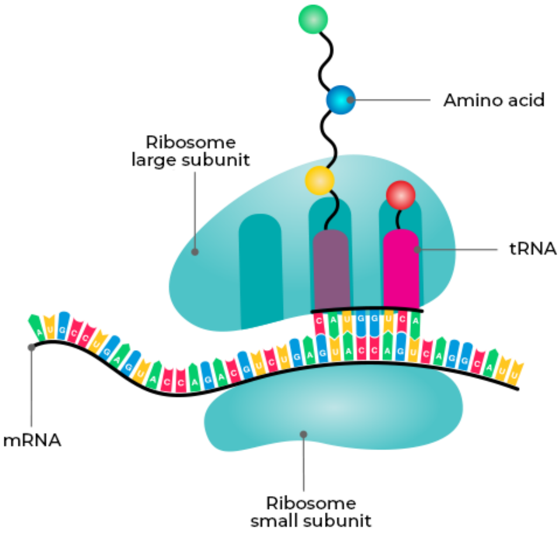

Figure 2.3: Structure of the ribosome, depicting the large and small subunits, which come together to translate mRNA into proteins. The ribosome has three main tRNA binding sites: the A site (aminoacyl), where new tRNAs bring in amino acids; the P site (peptidyl), where the growing polypeptide chain is held; and the E site (exit), where deacylated tRNAs leave the ribosome. The ribosome reads the mRNA in the 5' to 3' direction, coordinating the correct matching of tRNAs and forming peptide bonds to synthesize the polypeptide chain. Figure taken from "https://www.geeksforgeeks.org/ribosomes/".

2.3.1 Ribosome Scarcity in Biological Systems

The concentration of ribosomes often becomes limiting under various physiological and environmental conditions [10, 11, 12]. For instance, during times of cellular stress, such as nutrient deprivation or exposure to toxins, ribosome synthesis can be impaired, leading to a reduced pool of available ribosomes. Additionally, rapidly proliferating cells, such as those found in tumors or during embryonic development, can experience a shortage of ribosomes due to the high demand for protein synthesis, which outpaces ribosome production. Such situations highlight the importance of understanding how cells manage competition for ribosomes, especially under constrained conditions.

A clear example of the impact of ribosome scarcity can be observed in genetic engineering contexts, such as in *E. coli* engineered to produce large amounts of recombinant proteins like insulin. In these engineered strains, ribosome scarcity results from the significant metabolic burden of maintaining high-level expression of non-native genes [13]. Specifically, the engineered *E. coli* must allocate a substantial portion of its limited ribosomal pool to synthesize insulin, thereby reducing the availability of ribosomes for endogenous protein synthesis. This competition for ribosomes can severely impair bacterial growth, leading to a reduction in overall productivity due to slower cell division and increased metabolic stress.

The burden effect exemplifies the broader concept of resource competition, where the production of target proteins in engineered systems results in a trade-off between cellular growth and synthetic output. High expression levels of the insulin gene can overwhelm the host cell's ribosomal capacity, resulting in the accumulation of misfolded proteins and activation of stress response pathways. This stress can further exacerbate ribosome scarcity, triggering a cascade of metabolic costs that limit both cellular viability and protein yield. Strategies such as using regulated promoters, optimizing codon usage, and even engineering orthogonal ribosomes have been developed to mitigate these effects, helping to alleviate the resource burden and improve the balance between growth and recombinant protein production.

Investigating scenarios of low ribosome concentration helps capture the dynamics that cells face in these common biological contexts, both in natural and engineered systems. Such studies could reveal important principles of cellular regulation and resource allocation, as cells often need to efficiently manage limited resources. Understanding these dynamics is crucial not only for elucidating fundamental biological mechanisms but also for optimizing synthetic biology applications, where efficient resource utilization is key to maximizing productivity.

Chapter 3

Introduction to the Post-Transcriptional Gene Expression Oscillatory Model

The third chapter of this thesis introduces a post-transcriptional model of gene expression regulation that exhibits sustained oscillatory behavior under specific parameter sets. In particular, we demonstrate how miRNAs, which were introduced in the previous chapter, can generate stable oscillations in their target genes. This characteristic of miRNAs provides the first essential component for time-sharing: the presence of oscillators. This model, originally presented in the article "*Nonmodular oscillator and switch based on RNA decay drive regeneration of multimodal gene expression*" by Nordick et al. [2], forms the foundation for the development of the extended model explored in this thesis. The chapter will outline the structure of the model and describe the results obtained, establishing a basis for subsequent analysis and modifications.

3.1 Introduction to the Model

The model describes the regulatory dynamics occurring at the post-transcriptional level, particularly focusing on interactions between mRNA and miRNA. It involves an mRNA molecule with two binding sites for miRNA, where each binding site can independently engage with miRNA, resulting in the formation of two types of complexes: C_1, which involves a single bound miRNA, and C_2, where both binding sites are occupied. The presence of two binding sites is crucial, as it leads to sustained oscillatory behavior, which is absent in simpler versions of the model where only a single binding site is present.

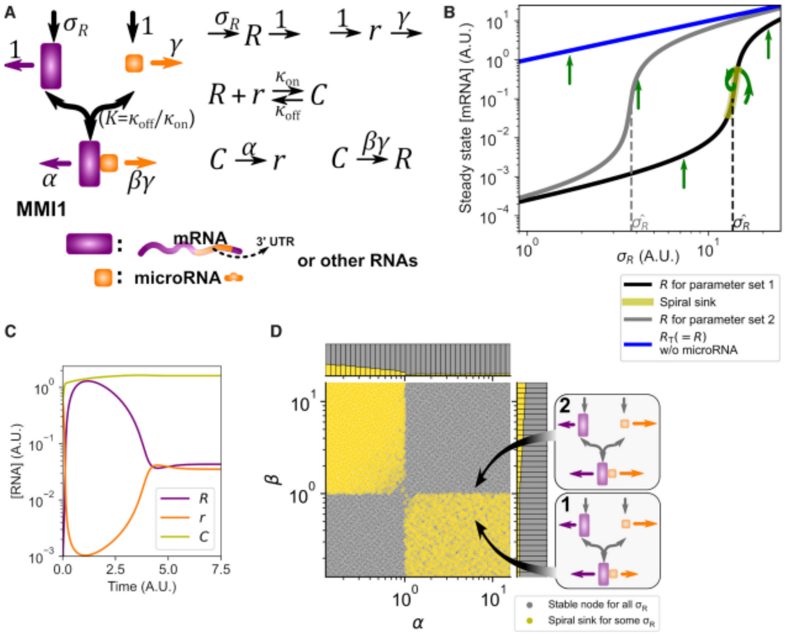

Figure 3.1: Dynamics of the MMI1 Model. (A) Left: Diagram illustrating the reaction network of the MMI1 model, which includes mRNA (represented by the purple box) and microRNA (represented by the orange box). Degradation processes are indicated by horizontal arrows, synthesis processes by vertical straight arrows, and binding by curved arrows. Right: Eight reactions associated with the MMI1 model, describing the formation and dissociation of mRNA-microRNA complexes under the law of mass-action. (B) Signal-response curves showing the steady state levels of unbound mRNA (R) in response to transcription rate constant σ_R. The green arrows illustrate the nature of these steady states: straight arrows indicate stable nodes, while spiral arrows represent spiral sinks. The blue curve illustrates the microRNA-free steady state response. (C) Time-course simulation illustrating transient oscillations that occur near a spiral sink steady state (using parameter set 1). The x-axis represents time in arbitrary units, approximately equivalent to $1.44 \times t_{1/2}$, where $t_{1/2}$ is the half-life of mRNA. (D) Parameter space illustrating the distribution of parameter sets: those capable of generating spiral sinks (yellow regions, as in parameter set 1) and those without (gray regions, as in parameter set 2). The parameter axes α and β represent degradation rate constants governing the behavior of the network. Representative diagrams of the two parameter sets are depicted on the right.

The model is built on two primary components: miRNA binding to mRNA at the two interaction sites, and the regulated degradation of RNA. These processes alone, without the involvement of explicit feedback loops, are sufficient to produce sustained oscillations. This oscillatory behavior emerges from a dynamic balance among the synthesis, binding, and degradation of both mRNA and miRNA, with miRNA-mediated degradation playing a central role. Bifurcation analysis and numerical simulations have demonstrated that the model can exhibit multistability and regenerate gene expression heterogeneity, potentially influencing cellular differentiation and providing cells with the ability to adapt to stress conditions.

This "heterogeneity restoration" means that the system can regenerate diverse patterns of gene expression across a population of cells, even if they start in a more uniform or synchronized state. The oscillatory dynamics produced by the interactions between mRNA and miRNA, particularly due to the presence of two miRNA binding sites, introduce temporal fluctuations in the levels of mRNA and miRNA. These fluctuations naturally lead to variations in gene expression among individual cells.

Such oscillatory behavior provides a mechanism for creating differences in expression levels across cells, contributing to heterogeneity. Moreover, in a population, even small differences in initial conditions or stochastic events can cause cells to fall out of sync with each other. Over time, this leads to a diverse set of expression states, restoring heterogeneity within the population. This property is highly relevant for biological functions like cellular differentiation and adaptation to stress, where maintaining a diverse range of cellular states increases the likelihood of survival and successful adaptation to changing conditions.

In the original paper, this model is referred to as MMI2, where "M" stands for mRNA, "M" for microRNA, and "I2" denotes the presence of two interaction sites. From now on, this thesis will refer to it as the MMI2 model.

3.1.1 Variants of the MMI2 Model and the Choice of the MMI2-SSB Model

There are several variants of the MMI2 model mentioned in the original paper by Nordick et al. [2], each providing a different perspective on the dynamics of mRNA and miRNA interactions. These variants include:

- **MMI2-SSB (Sequentially Symmetrical Binding)**: This variant assumes symmetric binding at both miRNA interaction sites, making it the simplest and most concise version. This model is chosen for its simplicity and effectiveness in capturing the complex dynamics with reduced computational complexity.
- **MMI2-ASB (Sequentially Asymmetrical Binding)**: Unlike the MMI2-SSB, this model assumes asymmetry in the binding characteristics of the two miRNA binding sites, which leads to potentially different kinetic behaviors

between the sites. This asymmetry adds additional complexity but can provide a more nuanced understanding of regulatory mechanisms.

- **MMI2-DMI (Dual miRNAs)**: This model incorporates interactions with two distinct miRNA species, which adds another layer of regulation. The dual miRNA binding can allow for more complex patterns of regulation and potentially diverse cellular responses.

In this thesis, the MMI2-SSB variant was chosen, as it represents the simplest and most concise version of this class of models. This simplified representation effectively captures the complex dynamics of the interactions while minimizing computational complexity.

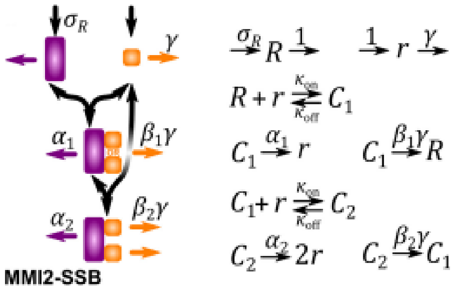

Figure 3.2: Figure adapted from [2]. Diagram of the MMI2-SSB model illustrating the interactions between mRNA (indicated as R and represented by a purple box), miRNA (indicated as r and represented by an orange box), and the formation of complexes C_1 and C_2. The complex C_1 is formed by the binding of R and r, and is represented in the figure as an intermediate complex. Similarly, C_2 is formed through further interaction involving C_1 and additional miRNA molecules. The arrows represent different reaction processes: the black arrows indicate complex formation and dissociation, while the colored arrows (purple and orange) represent activation and repression interactions, represented by different colors in order to distinguish between the interactions mediated by mRNA and miRNA, respectively. Parameters such as σ_R, α_1, β_1, α_2, and β_2 represent various rate constants governing the reactions. The right side of the figure provides a detailed representation of the reactions and the corresponding rate constants.

3.2 The Mathematical Model

The reactions in our MMI2-SSB model represented by Figure 3.2 can be summarized as follows:

1. **mRNA Synthesis**:

  - Reaction: $\emptyset \to R$
  - Rate: s_R (M/hr)

2. **mRNA Degradation**:
   - Reaction: $R \to \emptyset$
   - Rate: k_R^0 (1/hr)
3. **miRNA Synthesis**:
   - Reaction: $\emptyset \to r$
   - Rate: s_r (M/hr)
4. **miRNA Degradation**:
   - Reaction: $r \to \emptyset$
   - Rate: k_r^0 (1/hr)
5. **Association** (mRNA and miRNA binding to form complex C_1):
   - Reaction: $R + r \to C_1$
   - Rate: k_{on} (1/(Mhr))
6. **Dissociation** (Complex C_1 breaks into mRNA and miRNA):
   - Reaction: $C_1 \to R + r$
   - Rate: k_{off} (1/hr)
7. **Degradation of mRNA in Complex C_1**:
   - Reaction: $C_1 \to r$
   - Rate: k_R^1 (1/hr)
8. **Degradation of miRNA in Complex C_1**:
   - Reaction: $C_1 \to R$
   - Rate: k_r^1 (1/hr)
9. **Formation of Complex C_2** (binding of another miRNA to complex C_1):
   - Reaction: $C_1 + r \to C_2$
   - Rate: k_{on} (1/(Mhr))
10. **Dissociation of Complex C_2**:

  - Reaction: $C_2 \rightarrow C_1 + r$
  - Rate: k_{off} (1/hr)

11. **Degradation of mRNA in Complex C_2:**
  - Reaction: $C_2 \rightarrow 2r$
  - Rate: k_R^2 (1/hr)

12. **Degradation of miRNA in Complex C_2:**
  - Reaction: $C_2 \rightarrow C_1$
  - Rate: k_r^2 (1/hr)

The mathematical model is formulated using ordinary differential equations (ODEs) that describe the temporal evolution of the concentrations of mRNA (R), miRNA (r), and the related complexes (C_1 and C_2). The approach used is based on the law of mass action, which allows modeling the reaction rate as a function of the concentrations of the reactants. This approach enables precise representation of molecular interactions and facilitates the study of the dynamics of emerging oscillations.

$$\begin{aligned}
\frac{d\hat{R}}{dt} &= s_R - k_R^0\hat{R} - 2k_{on}\hat{R}\hat{r} + 2k_{off}\hat{C}_1 + 2k_r^1\hat{C}_1 \\
\frac{d\hat{r}}{dt} &= s_r - k_r^0\hat{r} - 2k_{on}\hat{R}\hat{r} + 2k_{off}\hat{C}_1 + 2k_R^1\hat{C}_1 - 2k_{on}\hat{C}_1\hat{r} + 2k_{off}\hat{C}_2 + 2k_R^2\hat{C}_2 \\
\frac{d\hat{C}_1}{dt} &= k_{on}\hat{R}\hat{r} - k_{off}\hat{C}_1 - k_R^1\hat{C}_1 - k_r^1\hat{C}_1 - k_{on}\hat{C}_1\hat{r} + k_{off}\hat{C}_2 + k_r^2\hat{C}_2 \\
\frac{d\hat{C}_2}{dt} &= 2k_{on}\hat{C}_1\hat{r} - 2k_{off}\hat{C}_2 - k_R^2\hat{C}_2 - 2k_r^2\hat{C}_2
\end{aligned} \tag{3.1}$$

The factor 2 in the differential equations of the MMI2-SSB model is present because the mRNA has two identical microRNA binding sites. Each site can bind or unbind independently, effectively doubling the rate of these interactions compared to a single-site model.

3.2.1 Adimensionalization

In this section, we proceed with adimensionalization similarly to the approach used in the referenced paper [2]. The purpose of adimensionalization is to simplify the mathematical analysis by removing dependence on specific units, making the model easier to work with and more generalizable. This process reduced the complexity of mathematical computations, making it easier to analyze the system's behavior and derive insights. To make this explicit, all parameters and variables have been rescaled in terms of the target's half-life (specifically, the mRNA degradation rate).

$R = \hat{R} \times \frac{k_R^0}{s_r}$	$r = \hat{r} \times \frac{k_r^0}{s_r}$	$C_1 = \hat{C_1} \times \frac{k_R^0}{s_r}$	$C_2 = \hat{C_2} \times \frac{k_R^0}{s_r}$

Table 3.1: Variables transformations used for adimensionalizing the equations.

$s_R \rightarrow \sigma_R$	$\sigma_R = \frac{s_R}{s_r}$
$k_R^0 \rightarrow \gamma_R$	$\gamma_R = 1$
$s_r \rightarrow \sigma_r$	$\sigma_r = 1$
$k_r^0 \rightarrow \gamma_r$	$\gamma_r = \frac{k_r^0}{k_R^0}$
$k_{on} \rightarrow \kappa_{on}$	$\kappa_{on} = \frac{k_{on} \times s_r}{(k_R^0)^2}$
$k_{off} \rightarrow \kappa_{off}$	$\kappa_{off} = \frac{k_{off}}{k_R^0}$
$k_R^1 \rightarrow \alpha_1$	$\alpha_1 = \frac{k_R^1}{k_R^0}$
$k_r^1 \rightarrow \beta_1 \gamma_r$	$\beta_1 = \frac{k_r^1}{k_r^0}$
$k_R^2 \rightarrow \alpha_2$	$\alpha_2 = \frac{k_R^2}{k_R^0}$
$k_r^2 \rightarrow \beta_2 \gamma_r$	$\beta_2 = \frac{k_r^2}{k_r^0}$

Table 3.2: Parameter transformations used for adimensionalizing the equations.

After adimensionalizing the system, the resulting differential equations describe the dynamics of mRNA (R), miRNA (r), and their associated complexes (C_1 and C_2) in a dimensionless form:

$$
\begin{aligned}
\frac{dR}{dt} &= \sigma_R - \gamma_R R - 2\kappa_{on} Rr + 2\kappa_{off} C_1 + 2\beta_1 \gamma_r C_1 \\
\frac{dr}{dt} &= \sigma_r - \gamma_r r - 2\kappa_{on} Rr + 2\kappa_{off} C_1 + 2\alpha_1 C_1 - 2\kappa_{on} C_1 r + 2\kappa_{off} C_2 + 2\alpha_2 C_2 \\
\frac{dC_1}{dt} &= \kappa_{on} Rr - \kappa_{off} C_1 - \alpha_1 C_1 - \beta_1 \gamma_r C_1 - \kappa_{on} C_1 r + \kappa_{off} C_2 + \beta_2 \gamma_r C_2 \\
\frac{dC_2}{dt} &= 2\kappa_{on} C_1 r - 2\kappa_{off} C_2 - \alpha_2 C_2 - 2\beta_2 \gamma_r C_2
\end{aligned}
\tag{3.2}
$$

3.3 Parameter Estimation

In this section, is described the process of parameter selection to render the models biologically plausible. The procedure involves using estimated median values based on experimental measurements, with the addition of a wide range of values to represent biological variability and measurement errors, covering at least two orders of magnitude for each parameter.

3.3.1 Basal Degradation Constants

- **mRNA:**
    - The mean half-life of mRNA without post-transcriptional control has been estimated to be approximately 4 hours in mammals [14]. The corresponding basal degradation constant k_R^0 is calculated as:

$$k_R^0 = \frac{\ln 2}{4\,\mathrm{hr}} = 0.17\,\mathrm{hr}^{-1}.$$

    - Although the parameter k_R^0 is not present explicitly in the adimensionalized ODEs—since in the dimensionless ODEs we use $\hat{t} = t/k_R^0$—it is important to consider its plausible range to establish the time unit in simulations. This corresponds on average to 5.88 hours but can vary from 7.14 minutes to 34.6 hours, depending on the stability of the mRNA [15, 16].
- **microRNA:**
    - The mean half-life of microRNAs has been estimated to be about four times that of mRNAs [17, 18]; therefore:

$$k_r^0 = \frac{\ln 2}{16\,\mathrm{hr}} = 4.3 \times 10^{-2}\,\mathrm{hr}^{-1}.$$

    - The basal degradation constant in the dimensionless model, γ_r, is thus calculated as $\gamma_r = 1/4$. Since in the dimensionless ODEs the parameter γ is sampled, an interval of $[10^{-1/4}, 10^{1/4}]$ was chosen using a log-uniform distribution to account for biological variability [2].

3.3.2 Synthesis Constants

- **mRNA:**
    - The synthesis constant of mRNA (s_R) is a control parameter that was varied to explore different dynamical behaviors of the model. The authors of [2] did not explicitly estimate s_R. But we investigated a range of biologically plausible values. First, the cytoplasmic volume of a murine myoblast was estimated as $V = 1.8 \times 10^{-12}\,\mathrm{L}$ ($1700\,\mu\mathrm{m}^3$) [19, 20], and average copy numbers for mRNA (in bacteria, yeast, and mammal cells were considered): $n_{\mathrm{bacteria}} = 5.1 \times 10^3$ [21], $n_{\mathrm{yeast}} = 1.22 \times 10^4$ [22],

and $n_{\text{mammal}} = 6.0 \times 10^5$ copies per cell [23]. Therefore, the estimated concentration is in the range:

$$\hat{r} = \frac{n}{N_A V} = 4.7 \times 10^{-9}\,\text{M to } 5.5 \times 10^{-8}\,\text{M},$$

where N_A is Avogadro's constant.

- Assuming that the mRNA has a degradation constant $k_r^0 = 0.17\,\text{hr}^{-1}$, the estimated synthesis constant is in the range:

$$s_R = k_r^0 \hat{r} = 8.0 \times 10^{-10}\,\text{M} \cdot \text{hr}^{-1}\,\text{to}\, 9.4 \times 10^{-9}\,\text{M} \cdot \text{hr}^{-1}.$$

The range of values is consistent with the range in which the authors of the article [2] vary the rate of mRNA synthesis.

- **microRNA:**
  - The synthesis constant of microRNA (s_r) is a scaling factor that does not explicitly appear in the dimensionless ODEs. To relate the scaled variables and parameters to realistic biological quantities, a representative value of s_r for a relatively abundant microRNA was considered. First, an average copy number of two highly expressed microRNAs was estimated as $n = 9.7 \times 10^3$ copies per cell [24]. Therefore, the estimated concentration for an abundantly expressed microRNA is:

$$\hat{r} = \frac{n}{N_A V} = 9.5 \times 10^{-9}\,\text{M},$$

where N_A is Avogadro's constant.

  - Assuming that the microRNA has a degradation constant $k_r^0 = 4.3 \times 10^{-2}\,\text{hr}^{-1}$, the estimated synthesis constant is:

$$s_r = k_r^0 \hat{r} = 4.1 \times 10^{-10}\,\text{M} \cdot \text{hr}^{-1}.$$

3.3.3 Association and Dissociation Constants

- The dissociation constant of the microRNA was estimated to be 3.7 pM [25]. The scaled dissociation constant K was then estimated using:

$$K = \frac{k_{\text{off}}}{k_{\text{on}}} \cdot \frac{k_R^0}{s_r} = 3.7 \times 10^{-12}\,\text{M} \times 0.17\,\text{hr}^{-1}/(4.1 \times 10^{-10}\,\text{M hr}^{-1}) \approx 1.5 \times 10^{-3},$$

where κ_{off} and κ_{on} represent the scaled dissociation and association rates, respectively. Given the significant variation in cell volume, RNA half-lives, microRNA concentration, and binding affinity, in [2] K were sampled from a range covering four orders of magnitude, i.e. $[1.5\times10^{-5}, 1.5\times10^{-1}]$, using a log-uniform distribution to account for biological variation and measurement errors. This range effectively encompasses scenarios in which there are approximately 10 copies of microRNA available for reactions in a cell, either due to low total concentration or occupancy by other mRNA targets.

- In order to estimate k_{on}, first consider the diffusion limit for k_{on}, i.e., $k_{\text{on}} \approx 3.6 \times 10^{13}\,\text{M}^{-1} \cdot \text{hr}^{-1}$ [26, 27]. However, to capture biological variability and measurement uncertainties, k_{on} was instead sampled from a range of values. A log-uniform distribution was used, ranging from $10^{12}\,\text{M}^{-1} \cdot \text{hr}^{-1}$ to $10^{14}\,\text{M}^{-1} \cdot \text{hr}^{-1}$, covering possible variations due to differences in diffusion conditions, local concentration effects, or changes in reaction environment [2].
- The scaled association rate constant κ_{on} was then calculated as:

  $$\kappa_{\text{on}} = k_{\text{on}} s_r / (k_R^0)^2,$$

  using the sampled range of k_{on}. Consequently, κ_{on} was also sampled from an interval calculated based on the k_{on} range, resulting in κ_{on} values ranging approximately from 5.1×10^4 to 5.1×10^6. This approach ensures that the variability in k_{on} propagates to the estimation of κ_{on}.
- The value of κ_{off} was subsequently estimated based on the representative value of κ_{on} and the estimated range of K mentioned above, i.e., $[7.7, 7.7 \times 10^4]$.

3.3.4 Regulated Degradation Factors (RDFs)

Regulated Degradation Factors (RDFs), denoted as α and β, are key parameters that regulate the degradation of mRNA and microRNA within molecular complexes, thereby influencing post-transcriptional gene expression dynamics. Specifically, α represents how fast mRNA is degraded in the complex relative to its unbound form, and β is the corresponding factor for microRNA. These RDFs are important because the gene regulatory function of microRNA primarily depends on the target mRNA degradation upon binding [28], and similarly, the target mRNA can alter the degradation rate constant of the mRNA-bound microRNA [29].

The assumption is made that mRNA and microRNA are degraded independently in the complex, supported by previous observations [29, 30, 31]. Such dynamics are crucial because they determine the system's ability to transition from simple dynamics to more complex behaviors, such as oscillations or bistability.

For instance, dynamics involving high ratios of degradation factors (α_2/α_1 and β_2/β_1) suggest significant functional cooperativity or synergy between the microRNA binding sites. A high α_2/α_1 ratio indicates that degradation is much faster when two binding sites are occupied compared to just one. This implies that when two microRNAs are bound, they collaborate more effectively to degrade mRNA, exhibiting positive cooperativity. Such behaviors can support oscillation, even without classic feedback circuits.

Experimental evidence highlights the importance of RDFs in shaping these dynamics. For example, mRNA destabilization driven by microRNA binding has been well-documented [28], and highly complementary targets can induce potent degradation of neuronal microRNAs [29]. Moreover, kinetic analyses reveal the complex interplay of microRNA and target degradation dynamics [30], and endogenous transcripts have been shown to control microRNA levels via target-directed degradation [31].

The regulated degradation factors α and β were sampled within the interval $[1/8, 16]$:

- The interval was chosen based on previous experimental data to cover a wide range of biological possibilities.
- Rare situations were also considered where the binding of the microRNA decreases the stability of the mRNA.
- Values were chosen using a log-uniform distribution to represent the variability of biological reactions.
- The median values of α and β are 1.4 and 0.35, respectively, at least two orders of magnitude smaller than κ_{off}.

Scaled parameter	Biological meaning	Estimated range
σ_R	Synthesis rate constant of mRNA	[0, 25]
γ	Degradation rate constant of miRNA	$[10^{-1/4}, 10^{1/4}]$
κ_{on}	Association constant	5.1×10^5
κ_{off}	Dissociation rate constant	$[7.7, 7.7 \times 10^4]$
α and β	Regulated degradation factor	[1/8, 16]

Table 3.3: Summary of scaled parameter values, their biological meaning, and estimated ranges used in the model.

Finally, sustained oscillations were identified using numerical bifurcation analysis and parameter sampling. By applying the total quasi-steady-state assumption (tQSSA) to complexes C_1 and C_2, the system reduced to a 2D Jacobian matrix, simplifying stability analysis. Stability was assessed by confirming that the eigenvalues of the 2D Jacobian matrix could be complex conjugates with negative real parts. Initial conditions were determined by performing phase plane analysis. The findings emphasized the importance of regulated degradation factors (RDFs) for both mRNA and miRNA, with cooperativity between binding sites being crucial. Oscillations were prevalent at high RDF ratios, while low RDF ratios required a high γ to induce oscillations [2].

3.4 Deterministic Results

The time-course trajectories presented in Figure 3.4 illustrate the sustained oscillations of mRNA (R), miRNA (r), and their complexes (C_1, C_2) over time. These results are consistent with the findings discussed in the paper "*Nonmodular oscillator and switch based on RNA decay drive regeneration of multimodal gene expression*" [2].

To reproduce the results presented in the paper, the following parameters and initial conditions were used in the MMI2-SSB model:

- **Parameters**:
  - $\sigma_R = 3.58$
  - $\gamma_R = 1$
  - $\sigma_r = 1$
  - $\gamma_r = 0.25$
  - $\kappa_{\text{on}} = 10^5$
  - $\kappa_{\text{off}} = 10^2$
  - $\alpha_1 = 1$
  - $\beta_1 = 1$
  - $\alpha_2 = 12$
  - $\beta_2 = 7$
- **Initial conditions**:
  - $R(0) = 3$
  - $r(0) = 0.75$
  - $C_1(0) = 0$
  - $C_2(0) = 0$

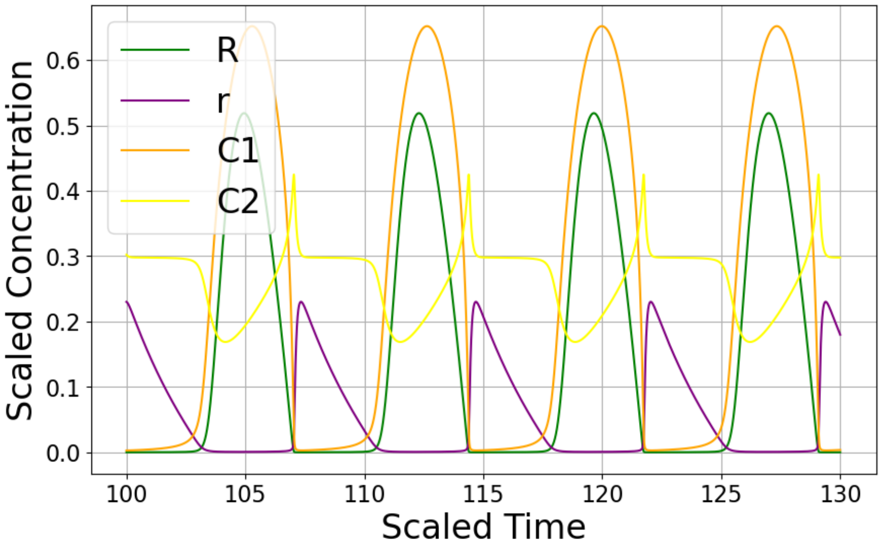

Figure 3.3: Sustained oscillations of mRNA, miRNA, and their complexes (R, r, C_1, C_2) as observed in the MMI2-SSB model. The curves were obtained by numerically integrating in Python the system of differential equations 3.2 over a time span of 100 units, with results presented for the last 30 time units.

3.5 Stochastic Results

In this work, the Gillespie algorithm was implemented to stochastically simulate the behavior of the MMI2-SSB model. This algorithm allows for the simulation of individual reaction events and the temporal evolution of the system, providing insight into the inherent variability of biological processes.

The Gillespie algorithm operates by simulating each reaction event individually, determining which reaction occurs next and how much time passes between reactions. The steps involved are:

1. **Calculate Propensities**: The propensity functions for each possible reaction are computed. These functions represent the likelihood of each reaction occurring in a very short time interval, given the current state of the system. The propensities used in this study for the twelve reactions of the MMI2-SSB model are as follows:
   - s_R: Production of R
   - $k_{R_0}R$: Degradation of R
   - s_r: Production of r
   - $k_{r_0}r$: Degradation of r

- $k_{on}Rr$: Formation of complex C_{1A}
- $k_{on}Rr$: Formation of complex C_{1B}
- $k_{off}C_{1A}$: Dissociation of complex C_{1A}
- $k_{off}C_{1B}$: Dissociation of complex C_{1B}
- $k_{R_1}C_{1A}$: Degradation of R in complex C_{1A}
- $k_{r_1}C_{1A}$: Degradation of r in complex C_{1A}
- $k_{R_1}C_{1B}$: Degradation of R in complex C_{1B}
- $k_{r_1}C_{1B}$: Degradation of r in complex C_{1B}
- $k_{on}(C_{1A} + C_{1B})r$: Formation of complex C_2
- $k_{off}C_2$: Dissociation of complex C_2
- $k_{R_2}C_2$: Degradation of R in complex C_2
- $k_{r_2}C_2$: Degradation of r in complex C_2

For the Gillespie algorithm, we differentiated between C_{1A} and C_{1B}, which represent complexes of mRNA with one miRNA, bound to the first and the second binding site respectively. This differentiation does not affect the overall dynamics, as both complexes function similarly, but it was necessary in the stochastic implementation to correctly simulate the binding events and ensure accurate tracking of the molecule states throughout the reactions.

2. **Determine Time to Next Reaction**: The time to the next reaction event is sampled from an exponential distribution, with a rate given by the sum of all propensities ($a_0 = \sum_{i=1}^{N} a_i$). The probability density function for the waiting time Δt is $P(\Delta t) = a_0 e^{-a_0 \Delta t}$, where a_0 is the total propensity. This allows for the correct stochastic timing of reaction events.

3. **Choose Which Reaction Occurs**: A specific reaction is chosen based on its propensity relative to the sum of all propensities. Specifically, the reaction is selected such that more likely reactions occur more often. This is achieved by generating a uniform random number between 0 and the total propensity (a_0), and then comparing this random value to the cumulative sum of propensities for each reaction. The reaction is chosen when the cumulative sum surpasses the random value, ensuring that reactions with higher propensities are more likely to be selected.

4. **Update State**: The state of the system is updated by changing the number of molecules involved in the chosen reaction. For example, if a complex is formed, the counts of the individual reactants are decreased, while the count of the complex is increased accordingly.

5. **Repeat**: Steps 1-4 are repeated until the simulation reaches a predefined stopping time, providing a temporal profile of the system's evolution.

In this work, Gillespie's algorithm was implemented using Python, allowing for the stochastic simulation of the twelve chemical reactions described above. The parameters and initial conditions used were the same as those outlined in the previous section, and the implementation relied on the known rate constants for production, degradation, association, and dissociation of the involved species. This allowed us to stochastically explore the behavior of the MMI2-SSB system and compare it with deterministic results obtained through ordinary differential equations (ODEs).

3.5.1 Changes in Variables

The Gillespie algorithm works with the number of individual particles. In this work, scaled parameters and variables were adapted so they would be compatible with the Gillespie algorithm.

- **Scaled to Real Parameters and Variables**: The parameters and concentrations were initially represented in a scaled, dimensionless form to simplify the mathematical modeling. These scaled values were then converted back to real biological units to enable meaningful biological interpretation.
- **Molar Concentrations to Number of Particles**: The molar concentrations were converted to actual molecule counts for each species. This conversion used known biological parameters such as the cytoplasmic volume and Avogadro's constant to translate concentrations into the number of particles for each molecular species.
- **Scaled Time to Real Time**: The scaled time was converted back to real time (in hours).

Multiple stochastic simulations were performed to observe variability in system behavior and compare these results with deterministic solutions. The number of stochastic simulations (N) was kept small due to computational challenges posed by the system's stiffness.

A stiff system has reactions with vastly different timescales, leading to a wide range of reaction rates. In the MMI2-SSB model, stiffness results from significant differences in reaction propensities. This makes accurate simulation with Gillespie's algorithm difficult, as it must handle very fast and slow reactions simultaneously, leading to inefficient and costly simulations.

Despite these challenges, the stochastic simulations show that the MMI2-SSB model exhibits rhythmic RNA concentration oscillations with notable variability, indicating that the model's oscillatory dynamics are robust even with molecular noise and stiffness.

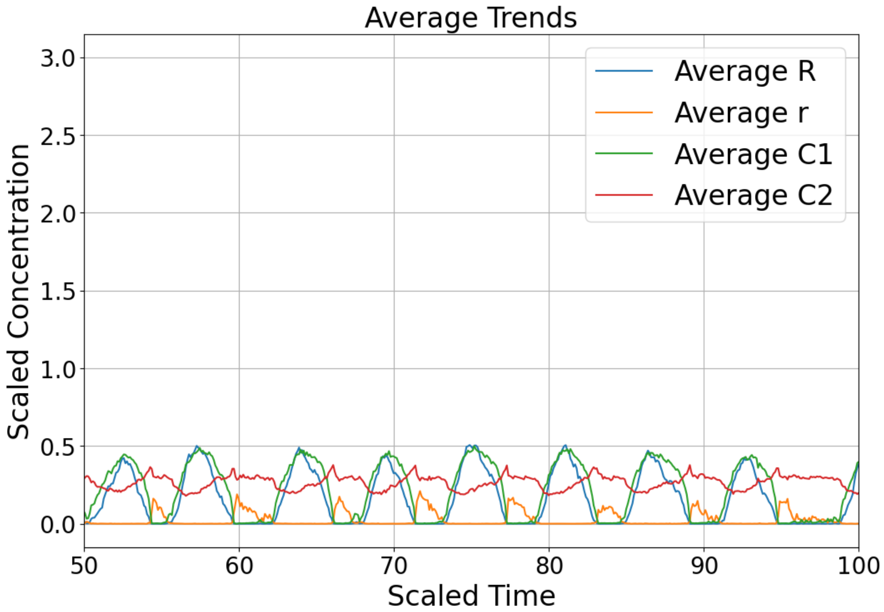

Figure 3.4: Stochastic trend showing the variability in concentration from 50 to 100 scaled hours for multiple stochastic simulations, using the Gillespie algorithm. The plot illustrates fluctuations around the deterministic trend, highlighting the effects of molecular noise. The average trend is obtained by averaging over $N = 100$ simulations.

3.6 Discussion of the Results

The observed oscillations highlight the intrinsic capacity of the MMI2-SSB model to produce rhythmic fluctuations in RNA species concentrations, even in the absence of explicit regulatory feedback loops [2].

In the next chapter, we will explore the possibility of having resource time-sharing when two of these miRNA-induced oscillators are coupled through a shared and limiting resource. In particular, we will analyze two independent MMI2-SSB systems in the presence of a shared pool of ribosomes. By systematically varying the ribosome concentration from low to abundant, we aim to investigate the behavior of these systems under shared-resource constraints. This exploration will focus on determining whether a time-sharing mechanism or other coordinated dynamics emerges between the two miRNA targets, particularly under conditions of limited ribosome availability.

Chapter 4

miRNA-mediated oscillators coupled through the ribosomal pool

4.1 Introduction

In this chapter, we will illustrate the model we developed to investigate the possibility of ribosome time-sharing induced by two miRNA-mediated oscillators. Indeed, the model consists of two independent MMI2-SSB systems, coupled through a fixed pool of ribosomes. This setup was designed to explore the dynamics that emerge from the competition between two systems that share a limited resource, specifically ribosomes, to determine if it is possible to observe time-sharing oscillations similar to those seen in other biological contexts [1, 3].

The reactions of this model are presented in Table 4.1.

The molecular species of type A and type B, if considered separately, present oscillatory dynamics resulting from post-transcriptional interactions via two miRNA binding sites. However, the innovative aspect of this model lies in introducing a fixed pool of ribosomes shared between the two systems. The two mRNAs of type A and B, will each "try to bind" ribosomes for protein translation, thus being effectively coupled through this shared pool.

	System A	**System B**
Synthesis of mRNA	$\emptyset \xrightarrow[s_R]{} R_A$	$\emptyset \xrightarrow[s_R]{} R_B$
Degradation of mRNA	$R_A \xrightarrow[k_R^0]{} \emptyset$	$R_B \xrightarrow[k_R^0]{} \emptyset$
Synthesis of miRNA	$\emptyset \xrightarrow[s_r]{} r_A$	$\emptyset \xrightarrow[s_r]{} r_B$
Degradation of miRNA	$r_A \xrightarrow[k_r^0]{} \emptyset$	$r_B \xrightarrow[k_r^0]{} \emptyset$
Formation of complex C_1	$R_A + r_A \xrightarrow[k_{on,A}]{} C_{1A}$	$R_B + r_B \xrightarrow[k_{on,B}]{} C_{1B}$
Dissociation of C_1	$C_{1A} \xrightarrow[k_{off}]{} R_A + r_A$	$C_{1B} \xrightarrow[k_{off}]{} R_B + r_B$
Degradation of mRNA in C_1	$C_{1A} \xrightarrow[k_R^1]{} r_A$	$C_{1B} \xrightarrow[k_R^1]{} r_B$
Degradation of miRNA in C_1	$C_{1A} \xrightarrow[k_r^1]{} R_A$	$C_{1B} \xrightarrow[k_r^1]{} R_B$
Formation of complex C_2	$C_{1A} + r_A \xrightarrow[k_{on,A}]{} C_{2A}$	$C_{1B} + r_B \xrightarrow[k_{on,B}]{} C_{2B}$
Dissociation of C_2	$C_{2A} \xrightarrow[k_{off}]{} C_{1A} + r_A$	$C_{2B} \xrightarrow[k_{off}]{} C_{1B} + r_B$
Degradation of mRNA in C_2	$C_{2A} \xrightarrow[k_R^2]{} 2r_A$	$C_{2B} \xrightarrow[k_R^2]{} 2r_B$
Degradation of miRNA in C_2	$C_{2A} \xrightarrow[k_r^2]{} C_{1A}$	$C_{2B} \xrightarrow[k_r^2]{} C_{1B}$
Formation of C	$R_A + Ribo \xrightarrow[k_{on,Ribo}]{} C_A$	$R_B + Ribo \xrightarrow[k_{on,Ribo}]{} C_B$
Dissociation of C	$C_A \xrightarrow[k_{off,Ribo}]{} R_A + Ribo$	$C_B \xrightarrow[k_{off,Ribo}]{} R_B + Ribo$

Table 4.1: Reactions of the model describing two miRNA targets coupled through a shared pool of ribosomes.

Our goal is to study whether competition for the fixed ribosomal pool can lead to time-sharing mechanisms, similarly to what observed in other biological contexts [1, 3]. If this is the case, such time-sharing mechanism could represent an advantageous strategy for resource allocation, allowing each mRNA to use ribosomes alternately thus reducing direct competition.

4.2 Mathematical Formalization of the Model

The mathematical model is formulated using ordinary differential equations (ODEs) that describe the temporal evolution of the concentrations of mRNA, miRNA, and their complexes for molecular species of type A and B, as well as the interactions with the shared ribosome pool. The equations have been extended from the original MMI2-SSB model in Chapter 3 to account for the simultaneous presence of two mRNAs competing for ribosomes, introducing terms that describe the binding and release rate of ribosomes by the two mRNAs.

$$
\begin{aligned}
\frac{dR_A}{dt} &= \sigma_R - \gamma_R R_A - 2\kappa_{\text{on}} R_A r_A + 2\kappa_{\text{off}} C_{1,A} + 2\beta_1 \gamma_r C_{1,A} - \kappa_{\text{on,Ribo}} R_A \, \mathit{Ribo} + \kappa_{\text{off,Ribo}} C_A \\
\frac{dr_A}{dt} &= \sigma_r - \gamma_r r_A - 2\kappa_{\text{on}} R_A r_A + 2\kappa_{\text{off}} C_{1,A} + 2\alpha_1 C_{1,A} - 2\kappa_{\text{on}} C_{1,A} r_A + 2\kappa_{\text{off}} C_{2,A} + 2\alpha_2 C_{2,A} \\
\frac{dC_{1,A}}{dt} &= \kappa_{\text{on}} R_A r_A - \kappa_{\text{off}} C_{1,A} - \alpha_1 C_{1,A} - \beta_1 \gamma_r C_{1,A} - \kappa_{\text{on}} C_{1,A} r_A + \kappa_{\text{off}} C_{2,A} + \beta_2 \gamma_r C_{2,A} \\
\frac{dC_{2,A}}{dt} &= 2\kappa_{\text{on}} C_{1,A} r_A - 2\kappa_{\text{off}} C_{2,A} - \alpha_2 C_{2,A} - 2\beta_2 \gamma_r C_{2,A} \\
\frac{dR_B}{dt} &= \sigma_R - \gamma_R R_B - 2\kappa_{\text{on}} R_B r_B + 2\kappa_{\text{off}} C_{1,B} + 2\beta_1 \gamma_r C_{1,B} - \kappa_{\text{on,Ribo}} R_B \, \mathit{Ribo} + \kappa_{\text{off,Ribo}} C_B \\
\frac{dr_B}{dt} &= \sigma_r - \gamma_r r_B - 2\kappa_{\text{on}} R_B r_B + 2\kappa_{\text{off}} C_{1,B} + 2\alpha_1 C_{1,B} - 2\kappa_{\text{on}} C_{1,B} r_B + 2\kappa_{\text{off}} C_{2,B} + 2\alpha_2 C_{2,B} \\
\frac{dC_{1,B}}{dt} &= \kappa_{\text{on}} R_B r_B - \kappa_{\text{off}} C_{1,B} - \alpha_1 C_{1,B} - \beta_1 \gamma_r C_{1,B} - \kappa_{\text{on}} C_{1,B} r_B + \kappa_{\text{off}} C_{2,B} + \beta_2 \gamma_r C_{2,B} \\
\frac{dC_{2,B}}{dt} &= 2\kappa_{\text{on}} C_{1,B} r_B - 2\kappa_{\text{off}} C_{2,B} - \alpha_2 C_{2,B} - 2\beta_2 \gamma_r C_{2,B} \\
\frac{dC_A}{dt} &= \kappa_{\text{on,Ribo}} R_A \, \mathit{Ribo} - \kappa_{\text{off,Ribo}} C_A \\
\frac{dC_B}{dt} &= \kappa_{\text{on,Ribo}} R_B \, \mathit{Ribo} - \kappa_{\text{off,Ribo}} C_B \\
\frac{d\mathit{Ribo}}{dt} &= -\kappa_{\text{on,Ribo}} (R_A + R_B) \, \mathit{Ribo} + \kappa_{\text{off,Ribo}} (C_A + C_B)
\end{aligned}
\tag{4.1}
$$

The species and rates are labeled as described in Section 3.2. Compared to 3.2, we introduce new variables: Ribo, representing free ribosomes, as well as complexes formed by ribosomes and mRNA species, along with their associated rates. Specifically, C_A and C_B represent complexes formed by ribosomes bound to the mRNA species R_A and R_B, respectively. The parameters $\kappa_{\text{on,Ribo}}$ and $\kappa_{\text{off,Ribo}}$ denote the association and dissociation rates of ribosomes to and from the mRNA.

The total quantity of ribosomes, denoted as Ribo_{tot}, remains constant. Thus, we have the conservation equation:

$$\mathit{Ribo}_{tot} = \mathit{Ribo} + C_A + C_B = \text{constant} \tag{4.2}$$

4.2.1 Parameters Estimation and Biologically Plausible Values for $k_{\text{on,Ribo}}$ and $k_{\text{off,Ribo}}$

This model extends the previous MMI2-SSB model discussed in Chapter 3 by including the association and dissociation reactions between free mRNA and ribosomes. Therefore, in this model, there are three additional chemical species: C_A, C_B, and *Ribo*, which represent the complex formed by type A mRNA with the ribosome, the complex formed by type B mRNA with the ribosome, and the ribosomes themselves, respectively. Additionally, there are two extra parameters,

$\kappa_{\text{on,Ribo}}$ and $\kappa_{\text{off,Ribo}}$, which are the scaled versions of $k_{\text{on,Ribo}}$ and $k_{\text{off,Ribo}}$. These represent the association rate between mRNA and ribosome and the rate of premature dissociation of the ribosome from the mRNA, respectively.

Estimation of $k_{\text{on,Ribo}}$

- The average cell volume is $V = 1.8 \times 10^{-12}\,\text{L}$ (1700 μm^3) as estimated in previous Chapter 3.
- The average number of ribosomes per cell is $N_{\text{Ribo}} = 5 \times 10^6$ [32].
- The concentration of ribosomes is calculated as:
  $$[\text{Ribo}] = \frac{N_{\text{Ribo}}}{N_A \times V} \approx 4.61\,\mu\text{M}$$
  where $N_A = 6.022 \times 10^{23}\,\text{mol}^{-1}$ is Avogadro's number.
- The initiation rate of translation is $k_{\text{init}} = 0.017$ to $0.167\,\text{s}^{-1}$ [33, 34].
- Calculate $k_{\text{on,Ribo}}$ using:
  $$k_{\text{on,Ribo}} = \frac{k_{\text{init}}}{[\text{Ribo}]}$$
- For the minimum value:
  $$k_{\text{on,Ribo}} = \frac{0.017}{4.61 \times 10^{-6}} \approx 3.69 \times 10^3\,\text{M}^{-1}\text{s}^{-1}$$
- For the maximum value:
  $$k_{\text{on,Ribo}} = \frac{0.167}{4.61 \times 10^{-6}} \approx 3.62 \times 10^4\,\text{M}^{-1}\text{s}^{-1}$$
- Converting to 1/(M*hr) by multiplying by 3600:
  $$k_{\text{on,Ribo}} \approx 1.06 \times 10^7 \text{ to } 1.04 \times 10^8\,1/(\text{M*hr})$$

Estimation of $k_{\text{off,Ribo}}$

- The premature dissociation rate of the ribosome from the mRNA, denoted as $k_{\text{off,Ribo}}$, has been estimated [35] as:
  $$k_{\text{off,Ribo}} = 0.24\,\text{min}^{-1}$$
- To convert this value to units of hr^{-1}:
  $$k_{\text{off,Ribo}} = 0.24\,\text{min}^{-1} \times 60\,\text{min/hr} = 14.4\,\text{hr}^{-1}$$
- We will consider a biologically plausible range for $k_{\text{off,Ribo}}$ that spans two orders of magnitude:
  $$k_{\text{off,Ribo}} \approx 1.44\,\text{to}\,144\,\text{hr}^{-1}$$

4.2.2 Adimensionalization

As done in the Section 3.2.1, the new variables in this model are also rescaled in the same way to make the ODEs 4.1.

$C_A = \hat{C}_A \times \frac{k_R^0}{s_r}$	$C_B = \hat{C}_B \times \frac{k_R^0}{s_r}$	$Ribo = \hat{Ribo} \times \frac{k_R^0}{s_r}$

Table 4.2: Variable transformations used for adimensionalizing the equations 4.1.

The new parameters are also rescaled accordingly.

$k_{\text{on,Ribo}} \rightarrow \kappa_{\text{on,Ribo}}$	$\kappa_{\text{on,Ribo}} = \frac{k_{\text{on,Ribo}} \times s_r}{(k_R^0)^2}$
$k_{\text{off,Ribo}} \rightarrow \kappa_{\text{off,Ribo}}$	$\kappa_{\text{off,Ribo}} = \frac{k_{\text{off,Ribo}}}{k_R^0}$

Table 4.3: Parameter transformations used for adimensionalizing the equations 4.1.

Calculation of Scaled Parameters

For $\kappa_{\text{on,Ribo}}$:

- Using $s_r = 4.1 \times 10^{-10}\,\text{M/hr}$ and $k_R^0 = 0.17\,\text{hr}^{-1}$.
- For $k_{\text{on,Ribo}} = 1.062 \times 10^7\,1/(\text{M*hr})$:

$$\kappa_{\text{on,Ribo}} = \frac{1.062 \times 10^7 \times 4.1 \times 10^{-10}}{(0.17)^2} \approx 1507$$

- For $k_{\text{on,Ribo}} = 1.044 \times 10^8\,1/(\text{M*hr})$:

$$\kappa_{\text{on,Ribo}} = \frac{1.044 \times 10^8 \times 4.1 \times 10^{-10}}{(0.17)^2} \approx 14796$$

For $\kappa_{\text{off,Ribo}}$:

- Using $k_R^0 = 0.17\,\text{hr}^{-1}$:
- For $k_{\text{off,Ribo}} = 1.44\,\text{hr}^{-1}$:

$$\kappa_{\text{off,Ribo}} = \frac{1.44}{0.17} \approx 8.47$$

- For $k_{\text{off,Ribo}} = 144\,\text{hr}^{-1}$:

$$\kappa_{\text{off,Ribo}} = \frac{144}{0.17} \approx 847$$

Therefore, the scaled parameters are:

- $\kappa_{\text{on,Ribo}} \approx 1507$ to 14796
- $\kappa_{\text{off,Ribo}} \approx 8.5$ to 847

Parameter	Scaled Range of Values
$\kappa_{\text{on,Ribo}}$	1507 to 14796
$\kappa_{\text{off,Ribo}}$	8.47 to 847

Table 4.4: Scaled parameters based on the adimensionalization shown in table 4.3.

4.3 Simulations and Results

In this section, we present the results obtained by numerically integrating the system of ODEs described in the System 4.1 from the previous section. We used Python 3.12.4 for the numerical integration within a time range of 0 to 300 time units, starting with the following initial conditions:

- $R(0) = 3$
- $r(0) = 0.75$
- $C_1(0) = 0$
- $C_2(0) = 0$
- $C_0(0) = 0$

All the parameters and initial values, except for the new ones introduced here, are exactly the same as those used in the simulations described in Section 3.2. Specifically, we added new binding/unbinding parameters for the ribosome pool, denoted as $\kappa_{\text{on,Ribo}}$ and $\kappa_{\text{off,Ribo}}$, as well as varied the initial concentration of the ribosomal pool itself ($Ribo(0) = Ribo_{tot}$).

The initial concentration of the ribosomal pool was varied across three representative values:

- $Ribo(0) = Ribo_{tot} = \{0, 0.5, 20\}$

This variation helps to analyze how changes in resource availability impact the dynamics of the system, particularly focusing on the emergence of oscillatory behavior.

The additional binding and unbinding parameters for the ribosomal pool, $\kappa_{\text{on,Ribo}}$ and $\kappa_{\text{off,Ribo}}$, were selected to ensure biological plausibility. The complete list of scaled parameters used in the simulations is as follows:

- $\sigma_R = 3.58$
- $\gamma_R = 1$
- $\sigma_r = 1$
- $\gamma_r = 0.25$
- $\alpha_1 = 1$
- $\beta_1 = 1$
- $\alpha_2 = 12$
- $\beta_2 = 7$
- $\kappa_{\text{on,A}} = 10000$
- $\kappa_{\text{off,A}} = 7.7$
- $\kappa_{\text{on,B}} = 10000$
- $\kappa_{\text{off,B}} = 7.7$
- $\kappa_{\text{on,Ribo}} = 15000$
- $\kappa_{\text{off,Ribo}} = 7.7$

Figure 4.1 shows two independent mRNA species, R_A and R_B, with two miRNA binding sites each, regulated by two independent miRNA, r_A and r_B respectively. The total amount of ribosomes is set to 0, $Ribo(0) = Ribo_{tot} = 0$. In this scenario, the trends corresponding molecular species A and B are undistinguishable, indeed they are equivalent, sharing the same parameters and initial conditions. In Figures 4.2 and 4.3, the two mRNAs are coupled by the presence of a ribosomal pool, which is greater than 0 ($Ribo(0) = Ribo_{tot} > 0$). We observe, however, that even in these scenarios the behaviors over time of the molecular species A and B are undistinguishable. Figure 4.2 shows the dynamics in presence of a limited (scaled) pool of ribosomes, $Ribo(0) = Ribo_{tot} = 0.5$, whereas Figure 4.3 shows the dynamics in presence of an abundant (scaled) ribosomal pool, $Ribo(0) = Ribo_{tot} = 20$. These results suggest that the presence of a ribosomal pool, regardless of its size, does not induce any observable difference between the two mRNA species A and B and their corresponding complexes, if they are completely indistinguishable from a deterministic point of view.

To investigate whether symmetry breaking between molecular species A and B could lead to different dynamic behaviors, asymmetry was introduced using two different values for $\kappa_{\mathrm{on,Ribo}}$ for mRNA A and B.

We set:

- $\kappa_{\mathrm{on,A}} = 10000$
- $\kappa_{\mathrm{on,B}} = 5000$

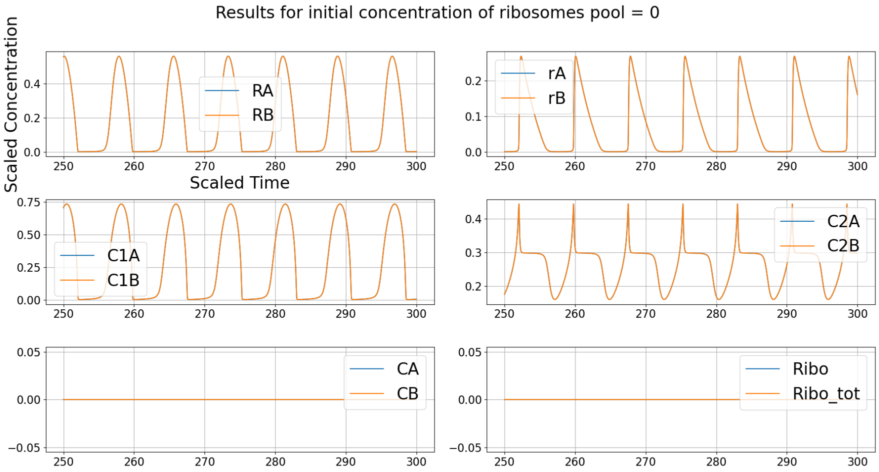

Figure 4.1: Dynamics of molecular species A and B with no initial ribosome pool ($Ribo(0) = Ribo_{tot} = 0$). Initial conditions and parameters were set to ensure complete symmetry between the two molecular species, leading to indistinguishable behavior in their dynamics. The plots were generated using Python 3.12.4 by numerically integrating the system of equations over the time interval [0, 300] and visualizing the results in the interval [250, 300].

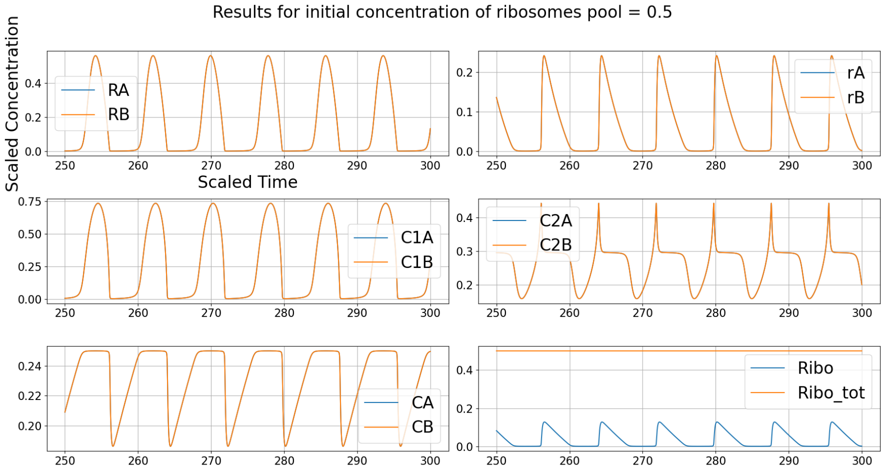

Figure 4.2: Dynamics of molecular species of type A and B with an initial ribosome pool of 0.5 ($Ribo(0) = Ribo_{tot} = 0.5$). The simulations were performed using the same method of Figure 4.1. Despite the limited ribosome pool, the dynamics of molecular species A and B remain synchronized and indistinguishable. This is because, in the absence of distinguishing factors, molecular species of type A and B behave as if they were identical entities arbitrarily assigned different labels, even under resource competition.

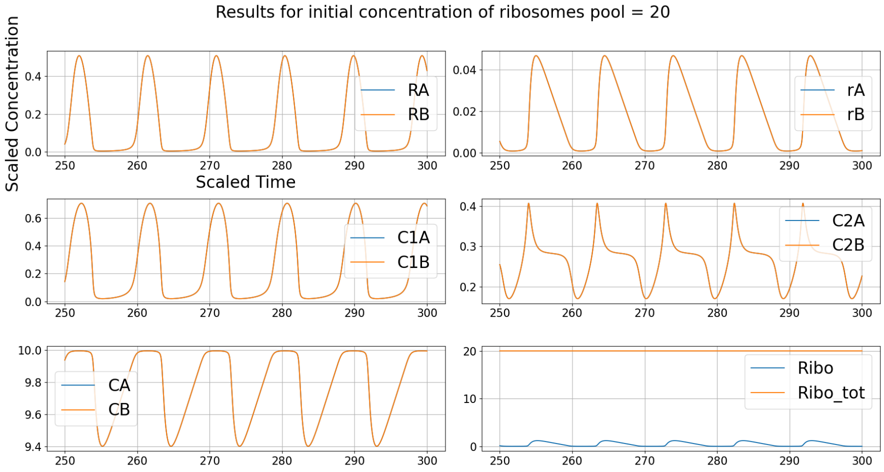

Figure 4.3: Dynamics of molecular species of type A and B with an initial ribosome pool of 20 ($Ribo(0) = Ribo_{tot} = 20$). The simulations were performed using the same method of Figure 4.1. Initial conditions and parameters were set to ensure complete symmetry between the two molecular species, leading to indistinguishable behavior in their dynamics.

Figures 4.4, 4.5, 4.6, illustrate the dynamics of molecular species A and B under different initial conditions for the ribosomal pool. These conditions include no availability of ribosomes, ($Ribo(0) = Ribo_{tot} = 0$), a limited ribosome pool ($Ribo(0) = Ribo_{tot} = 0.5$), and an abundant ribosome pool ($Ribo(0) = Ribo_{tot} = 20$). By comparing these scenarios, we can observe how the availability of ribosomes affects the synchronization and competition between molecular species A and B.

In Figure 4.4, R_A and R_B are once again decoupled by setting $Ribo(0) = Ribo_{tot} = 0$. However, in this case, the variation of the parameter $\kappa_{\text{on,Ribo,B}}$ with respect to $\kappa_{\text{on,Ribo,A}}$ has generated trends that are no longer overlapping. Instead, we observe differences in initial amplitude, period, and phase between molecular species A and B.

In Figures 4.5 and 4.6, the presence of a common pool of ribosomes, whether limiting or abundant, has eliminated the differences in period and phase between type A and type B for all chemical species, except for C_A and C_B. Specifically, when the ribosomal pool is limited ($Ribo(0) = Ribo_{tot} = 0.5$), as seen in Figure 4.5, there is a clear phase difference between C_A and C_B, indicating that R_A and R_B compete for the limited ribosome resource, and this results in a time-sharing mechanism in the dynamics of the complexes C_A and C_B. As expected, when the ribosomal pool is abundant ($Ribo(0) = Ribo_{tot} = 20$), as shown in Figure 4.6, the phase difference between C_A and C_B vanishes.

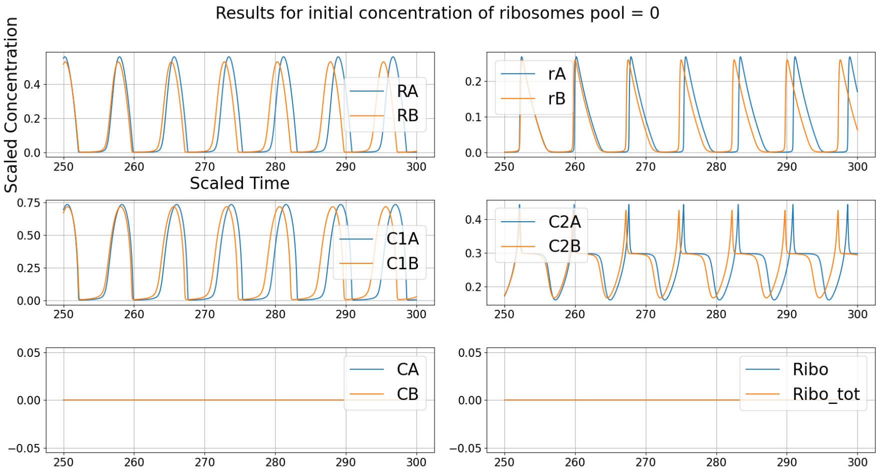

Figure 4.4: Dynamics of molecular species A and B with no initial ribosome pool ($Ribo(0) = Ribo_{tot} = 0$). The simulations were performed using the same method of Figure 4.1. Parameter asymmetry between $\kappa_{\text{on,A}}$ and $\kappa_{\text{on,B}}$ generates differences in the amplitude, period, and phase of the dynamics.

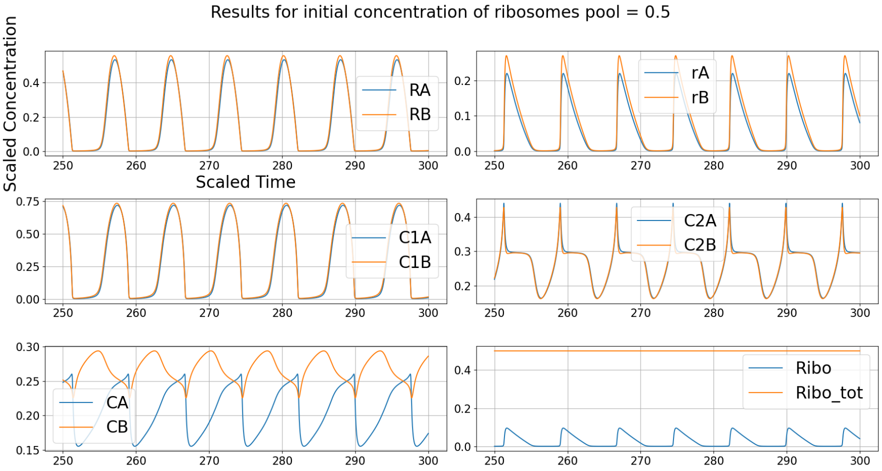

Figure 4.5: Dynamics of molecular species A and B with a limited ribosome pool ($Ribo(0) = Ribo_{tot} = 0.5$). The simulations were performed using the same method of Figure 4.1. The introduction of a shared, limited ribosome pool induces competition between R_A and R_B, resulting in a phase difference in the dynamics of the ribosome-bound complexes C_A and C_B. This time-sharing behavior highlights resource allocation effects under constrained conditions.

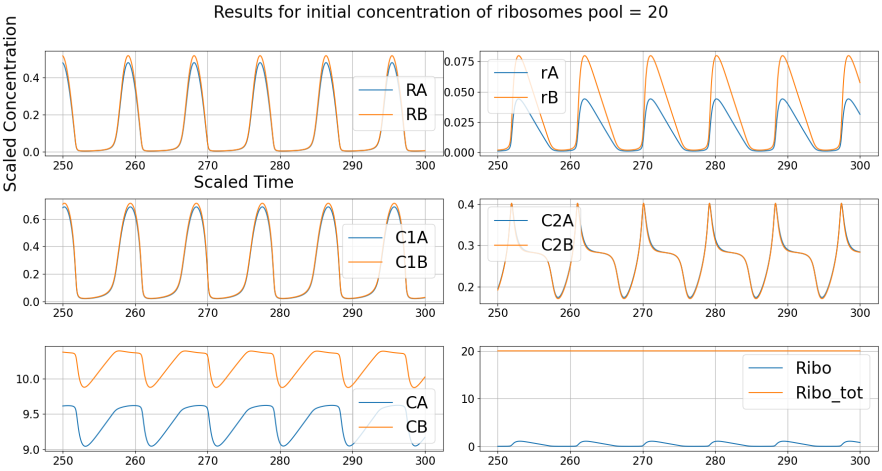

Figure 4.6: Dynamics of molecular species A and B with an abundant ribosome pool ($Ribo(0) = Ribo_{tot} = 20$). The simulations were performed using the same method of Figure 4.1. The availability of an excess ribosome pool eliminates phase differences between C_A and C_B, leading to synchronized dynamics across all molecular species. The effects of competition observed in Figure 4.5 are no longer present, as the ribosome resource is no longer limiting.

However, we expected that introducing asymmetry might lead to an anti-phase trend in the dynamics of the mRNAs themselves, R_A and R_B, when the molecular species A and B share a limited pool of ribosomes. Surprisingly, the results do not show a significant phase difference between the mRNAs R_A and R_B in presence of a limited pool of ribosomes. Instead, what emerges is an anti-phase dynamics involving only the mRNA-ribosome complexes, C_A and C_B. This suggests that the ribosome-mRNA interactions induce phase differentiation at the level of the mRNA-ribosome complexes, while the free mRNAs R_A and R_B remain largely synchronized. This finding highlights that the ribosome binding competition primarily affects the dynamics at the level of the complexes C_A and C_B, rather than altering the phase relationship of the free mRNAs.

Then, we reproduced the same plots as those presented previously, but with different parameter values that are not necessarily biologically plausible. This exploration aims to determine if these parameter changes result in similar oscillatory dynamics. In particular, we used the following parameter values:

- $\kappa_{\mathrm{on,A}} = 200$
- $\kappa_{\mathrm{off,A}} = 0.1$
- $\kappa_{\mathrm{on,B}} = 300$
- $\kappa_{\mathrm{off,B}} = 0.1$
- $\kappa_{\mathrm{on,Ribo}} = 1000$
- $\kappa_{\mathrm{off,Ribo}} = 1$

These parameter values are easier to handle computationally since they do not differ significantly in terms of orders of magnitude, making the system less stiff. A less stiff system facilitates numerical integration and reduces computational challenges, such as convergence issues or excessively small time steps that would otherwise be required for a highly stiff system. Despite these modifications, the results show that the oscillatory dynamics observed earlier are still present.

The results are shown in Figures 4.7, 4.8, and 4.9. These plots illustrate the dynamics of molecular species A and B for different initial concentrations of the ribosome pool: $Ribo(0) = Ribo_{tot} = 0$, $Ribo(0) = Ribo_{tot} = 0.5$, and $Ribo(0) = Ribo_{tot} = 20$, respectively.

Despite the less biologically plausible parameter values, the trends remain qualitatively similar to those obtained with biologically accurate parameters. We still observe synchronized dynamics for all chemical species under high ribosome availability and anti-phase behavior of ribosome-mRNA complexes when the ribosome pool is limited. These findings reinforce the robustness of the observed dynamics, which seem to persist across a wide range of parameter values.

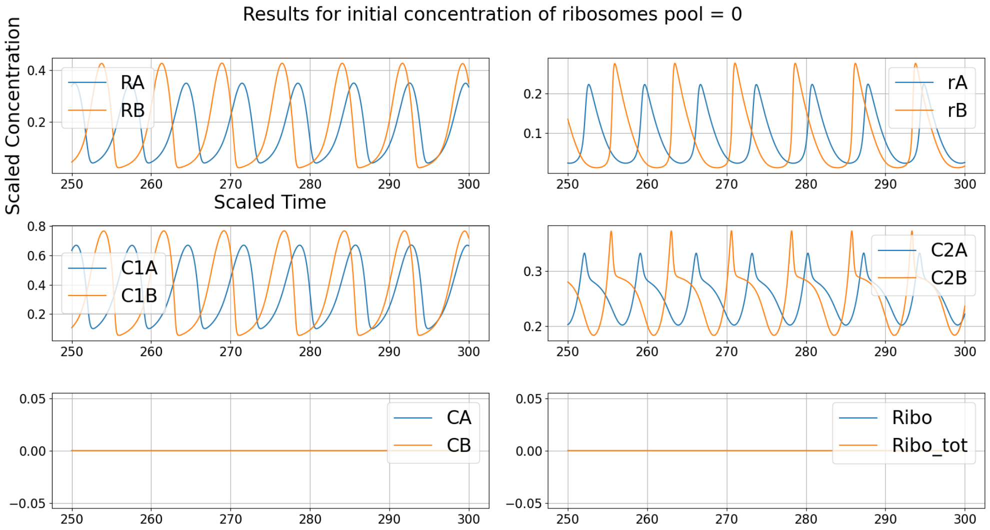

Figure 4.7: Dynamics of molecular species A and B with no initial ribosome pool ($Ribo(0) = Ribo_{tot} = 0$) using modified parameter values. The simulations were performed with the same method as Figure 4.1. The parameter asymmetry generates distinct oscillatory dynamics with no shared ribosome competition.

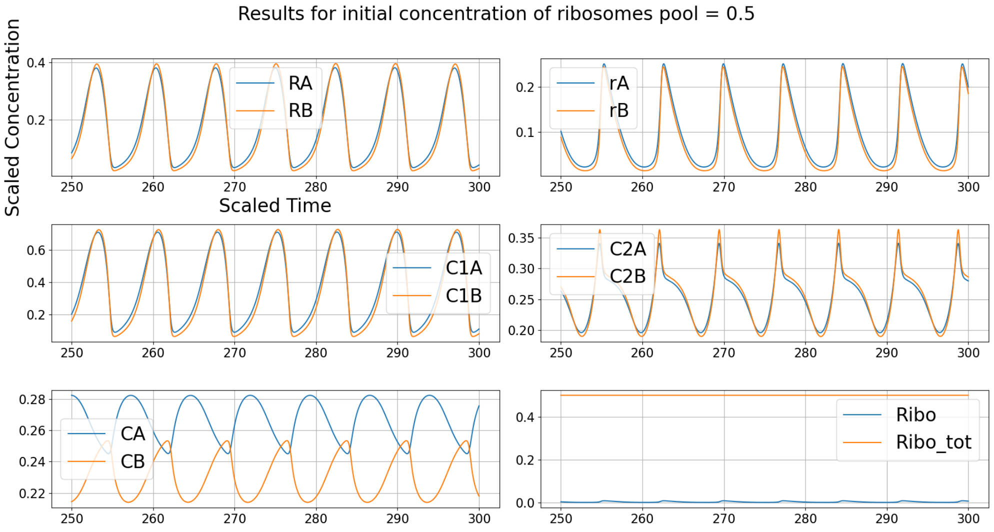

Figure 4.8: Dynamics of molecular species A and B with a limited ribosome pool ($Ribo(0) = Ribo_{tot} = 0.5$) using modified parameter values. The simulations were performed using the same method as Figure 4.1. The competition for ribosomes results in anti-phase behavior of the ribosome-mRNA complexes C_A and C_B.

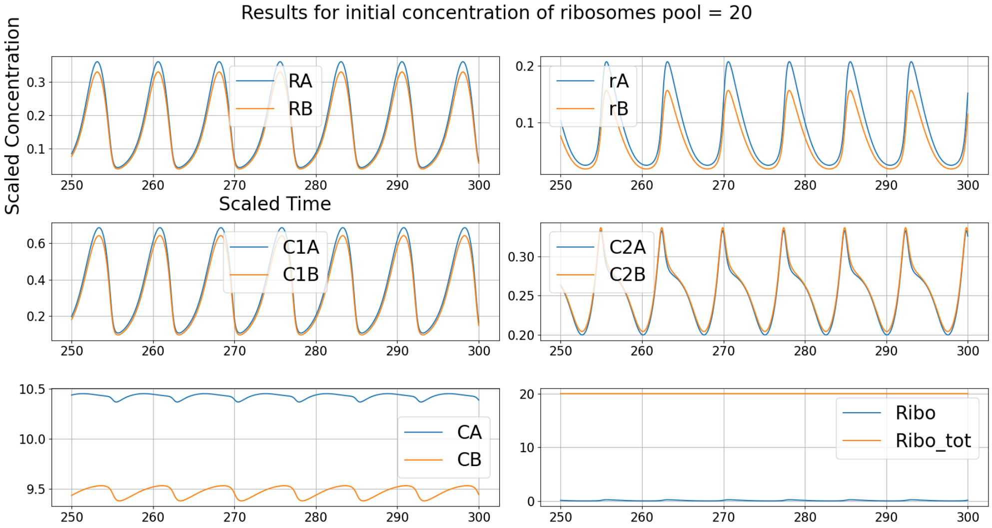

Figure 4.9: Dynamics of molecular species A and B with an abundant ribosome pool ($Ribo(0) = Ribo_{tot} = 20$) using modified parameter values. The simulations were performed using the same method as Figure 4.1. The high availability of ribosomes eliminates competition effects, leading to synchronized dynamics.

To better illustrate the initial dynamics before reaching a steady state, we focused on the initial time units. The following figures depict the behavior of the complexes C_A and C_B for the same initial ribosome concentrations as above (0.5 and 20), but zoomed in on the initial phase.

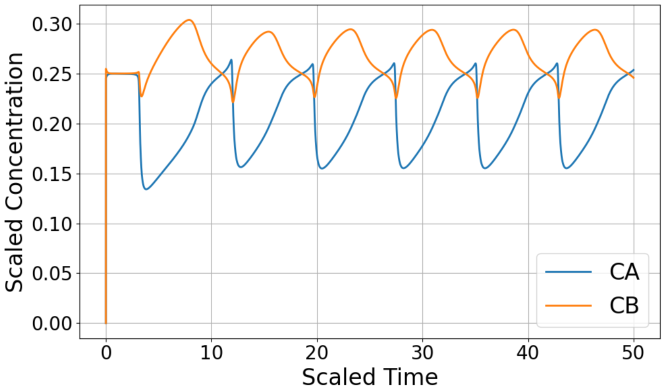

Figure 4.10: Initial dynamics of C_A and C_B with an initial ribosome pool of 0.5 ($Ribo(0) = Ribo_{tot} = 0.5$). A hierarchy is established during the initial time units where the least repressed mRNA (type A in this case) binds first and forms the majority of the complexes.

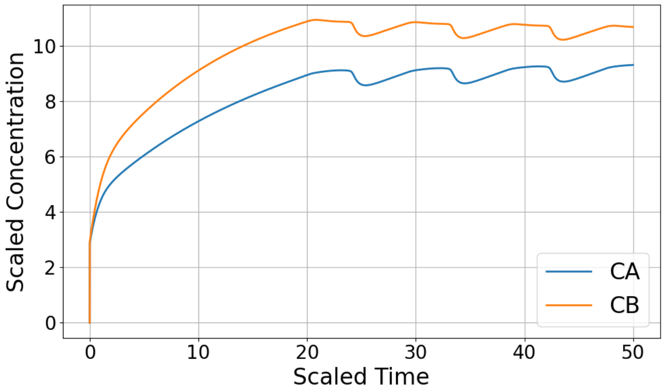

Figure 4.11: Initial dynamics of C_A and C_B with an initial ribosome pool of 20 $(Ribo(0) = Ribo_{tot} = 20)$. Both complexes rapidly reach a in-phase dynamics.

What one can observe is that, when the initial ribosomal pool concentration is low, a sort of hierarchy is established, whereby the least repressed mRNA (which for the first set of parameters is A and for the second it is B) immediately begins to bind to the ribosome, ensuring the largest fraction of ribosomes forming the complex, while the second mRNA gradually binds as more ribosomes become available. This initial dynamics creates an imbalance that can persist for a significant portion of the transient period, leading to the observed phase differences.

Additionally, it is notable that the second mRNA predominantly starts to binding during the dissociation period of the first mRNA. This means that when the complexes formed by the initially bound mRNA begin to dissociate, ribosomes become available, allowing the second mRNA to bind and form new complexes. This sequence of dissociation and binding further reinforces the observed time-sharing mechanism between the two mRNAs. This interplay of binding during dissociation allows the second mRNA to use the ribosomal pool when it becomes transiently free, leading to the staggered oscillatory behavior seen in the early stages.

When the available ribosomal pool is abundant $(Ribo(0) = Ribo_{tot} = 20)$, the initial dynamics is characterized by rapid binding of both mRNAs, leading to synchronized complex formation. The competition for ribosomes is effectively mitigated, and the molecular species of both type A and type B proceed with nearly identical concentrations. This behavior suggests that an ample supply of ribosomes effectively removes the competitive edge that one mRNA might have over the other, resulting in synchronized dynamics without a significant hierarchical advantage.

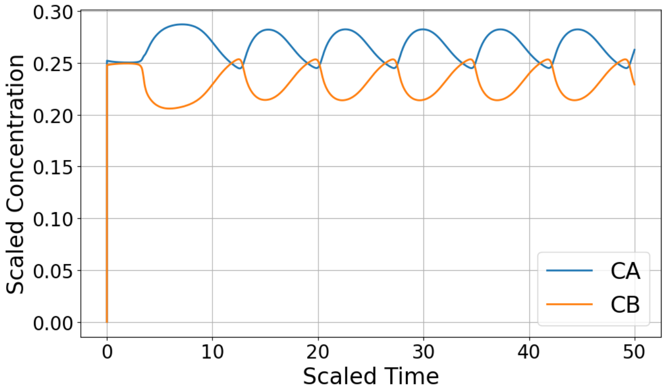

Figure 4.12: Initial dynamics of C_A and C_B with an initial ribosome pool of 0.5 ($Ribo(0) = Ribo_{tot} = 0.5$) using different parameter values. The least repressed mRNA (type B in this case) binds first, establishing a dominance in ribosome usage.

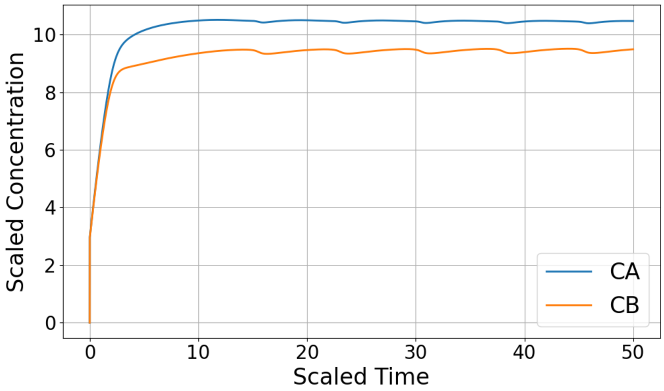

Figure 4.13: Initial dynamics of C_A and C_B with an initial ribosome pool of 20 ($Ribo(0) = Ribo_{tot} = 20$) using different parameter values. Despite the initial differences, synchronization is achieved quickly due to ample ribosome availability.

Then, we focused on the coupling between type A and type B species-except for C_A and C_B that we analyzed before-due to the presence of ribosomes by calculating the change in period. The following results summarize the periods of different species for different initial ribosome pool concentrations.

Set	$Ribo_{tot}$	R_A	R_B	r_A	r_B	C_{1A}	C_{1B}	C_{2A}	C_{2B}
Set 1	0	7.748	7.511	7.748	7.511	7.748	7.511	7.748	7.511
	0.5	7.721	7.721	7.721	7.721	7.721	7.721	7.721	7.721
	20	9.107	9.108	9.107	9.107	9.107	9.108	9.108	9.107
Set 2	0	7.035	7.578	7.035	7.575	7.035	7.575	7.036	7.575
	0.5	7.332	7.332	7.332	7.332	7.332	7.332	7.332	7.332
	20	7.485	7.485	7.485	7.485	7.485	7.485	7.485	7.485

Table 4.5: Periods for different $Ribo(0) = Ribo_{tot}$ values and parameter sets.

These results highlight that the introduction of the ribosome pool affects the synchronization and period of the oscillatory behavior of type A and type B species. For both sets of parameters, before introducing the ribosomal pool, there is a difference in period between type A and type B for each species induced by the specific miRNA-mRNA binding rates. However, once the two mRNA molecules are coupled through the ribosomes, the signals become synchronized with a period that lay between the two original periods. Indeed, the shared ribosomal pool effectively couples the dynamics of molecular species A and B, leading to their synchronized oscillations.

To further illustrate our findings, we present a set of summary plots that help visualize the phase differences across different initial conditions of the ribosome pool for both parameter sets.

The first plot (Figure 4.14) corresponds to the first set of biologically plausible parameters, while the second plot (Figure 4.15) represents the results for the second set of parameters, which are not necessarily biologically plausible. Despite the differences in parameter sets, both plots show qualitatively similar behavior. As ribosome availability increases, the phase difference between the complexes C_A and C_B decreases in both cases, suggesting the transition from an anti-phase oscillation to an in-phase oscillation. This indicates the robustness of the dynamics and the consistency of the system's response to increased ribosomal pool, regardless of the parameter set.

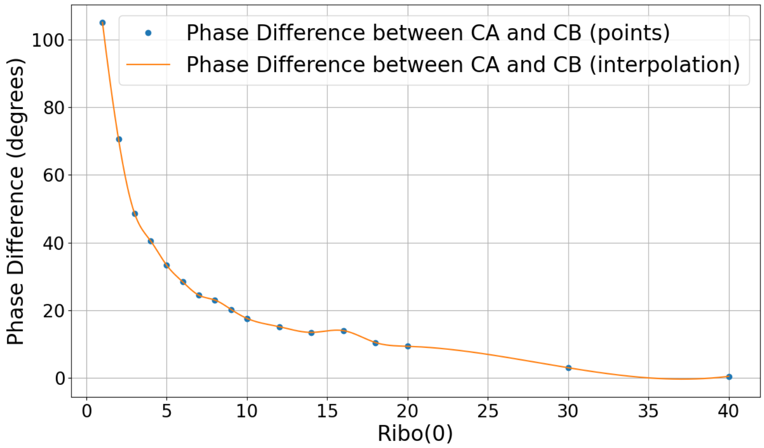

Figure 4.14: Phase difference between the complexes C_A and C_B as a function of the initial ribosomal pool concentration ($Ribo(0)$) for the first set of parameters. The phase difference is computed in Python using the Fourier Transform (FFT) to determine the phase angles of the dominant frequency components of C_A and C_B. The red point represents the phase difference when $Ribo(0) = 0$, while the orange curve illustrates the decreasing phase difference trend with increasing ribosome availability.

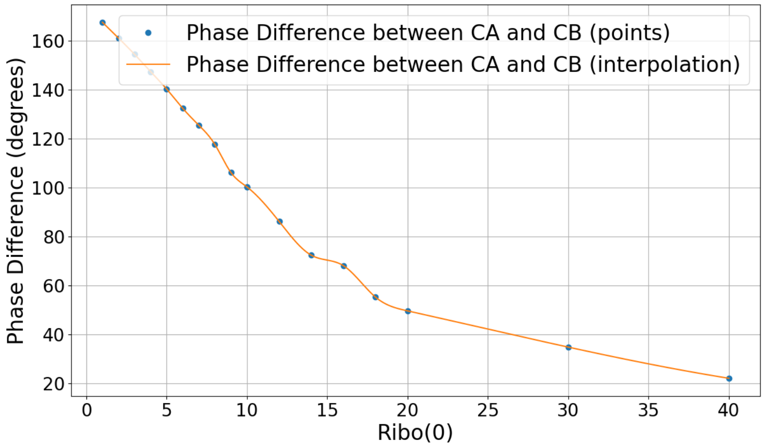

Figure 4.15: Phase difference between the complexes C_A and C_B as a function of the initial ribosome pool concentration ($Ribo(0) = Ribo_{tot}$) for the second set of parameters. The phase difference is computed exactly as described in Figure 4.14.

4.4 Proteins Production

In our study, we focused on analyzing the trends of C_A and C_B, which are the complexes formed by type A and type B mRNAs with ribosomes. These complexes are crucial intermediates that directly lead to protein production. By analyzing the dynamics of C_A and C_B, we can therefore infer the behavior of the proteins produced from these mRNAs.

Under certain conditions, especially when the amount of ribosomes is limited (e.g., $Ribo(0) = 0.5$), the trends of C_A and C_B exhibit time-sharing dynamics. This suggests that type A and type B proteins are produced alternately.

On the other hand, when ribosome availability is abundant (e.g., $Ribo(0) = 20$), the C_A and C_B dynamics become in-phase, leading to simultaneous production of both type A and type B proteins. In this case, ribosome competition is minimal, and both mRNAs can be translated concurrently, resulting in synchronized protein production [36].

Thus, we can assume that under these conditions—whether with limited or abundant ribosome availability—the dynamics of the produced proteins (both type A and B) follow exactly those of the ribosome-mRNA complexes (C_A and C_B). This highlights the critical role of ribosome availability in determining whether protein production follows an alternating or concurrent mode.

It makes sense to hypothesize that the trend of the produced proteins faithfully follows that of the complexes C_A and C_B, but this depends on the rates of protein production and degradation, denoted by σ_P (rate of production) and γ_P (rate of degradation), respectively. Specifically:

- If the rate of protein production (σ_P) is sufficiently high compared to the dynamics of complex formation, and the degradation rate (γ_P) is moderate or low, then the protein concentration will closely follow the trend of the complexes, with a slight delay due to the time required for translation [37].
- When γ_P is low, proteins accumulate and maintain a concentration profile that reflects the dynamics of the complexes over time, though with a small delay [37].
- If γ_P is high (indicating rapid protein degradation), the protein levels may not faithfully mirror the dynamics of C_A and C_B, as degradation may outpace production, leading to dampened oscillations or reduced amplitude [37].

Therefore, the dynamics of protein production will be consistent with those of C_A and C_B, with the main difference being a slight delay, provided that σ_P is sufficiently high and γ_P is not excessively large. This slight delay is an intrinsic feature of the translation process, as it takes time for ribosomes to produce proteins after forming the complexes.

4.5 Discussion

The emergence of anti-phase oscillatory behavior in this coupled mRNA-ribosome system is an adaptation, particularly for the more repressed mRNA. Under conditions of limited ribosome availability, the dynamics of competition between type A and type B mRNAs lead to an outcome where each type takes turns in binding with the shared ribosome pool.

When both mRNAs oscillate in phase, they compete simultaneously for ribosomes. In this scenario, the more repressed mRNA is inherently at a disadvantage because it has a lower likelihood of ribosome recruitment compared to the less repressed mRNA. Since both mRNAs are actively seeking ribosomes at the same time, the less repressed mRNA tends to dominate ribosome binding, resulting in a reduced share of ribosomes for the more repressed mRNA. Essentially, simultaneous competition skews resource allocation in favor of the mRNA that can initiate complex formation more effectively.

In contrast, the anti-phase oscillatory behavior provides an opportunity for the more repressed mRNA to gain access to ribosomes when the less repressed mRNA is in its dissociation phase. This temporal separation mitigates the direct competition between the two mRNAs. By oscillating out of phase, the more repressed mRNA can effectively "wait" until the ribosomes become available again, during the time when the less repressed mRNA's complexes are dissociating. This means that ribosomes are freed from one mRNA at the same time as the other mRNA becomes primed to bind, creating a rhythm of alternating usage.

Chapter 5

miRNA Sharing Model

In this chapter, we analyze a new system consisting of two types of mRNA that share the same type of miRNA. Unlike Chapter 4, where mRNA types A and B were regulated by separate miRNAs, here both mRNA type A and type B share the same miRNA. This model aims to reflect the reality of cellular environments, where the same miRNA often regulates multiple distinct mRNAs [38], thus eliminating the separation between different types of miRNAs. The model setup involves two mRNAs, coupled through a shared miRNA and a common pool of ribosomes.

5.1 Mathematical Formalization of the Model

The following ODEs represent the dynamics of the model:

$$\begin{aligned}
\frac{dR_A}{dt} &= \sigma_R - \gamma_R R_A - 2\kappa_{\text{on,A}} R_A r + 2\kappa_{\text{off,A}} C_{1,A} + 2\beta_1 \gamma_r C_{1,A} - \kappa_{\text{on,Ribo}} R_A \text{Ribo} + \kappa_{\text{off,Ribo}} C_A \\
\frac{dR_B}{dt} &= \sigma_R - \gamma_R R_B - 2\kappa_{\text{on,B}} R_B r + 2\kappa_{\text{off,B}} C_{1,B} + 2\beta_1 \gamma_r C_{1,B} - \kappa_{\text{on,Ribo}} R_B \text{Ribo} + \kappa_{\text{off,Ribo}} C_B \\
\frac{dr}{dt} &= \sigma_r - \gamma_r r \\
&\quad - 2\kappa_{\text{on,A}} R_A r + 2\kappa_{\text{off,A}} C_{1,A} + 2\alpha_1 C_{1,A} - 2\kappa_{\text{on,A}} C_{1,A} r + 2\kappa_{\text{off,A}} C_{2,A} + 2\alpha_2 C_{2,A} \\
&\quad - 2\kappa_{\text{on,B}} R_B r + 2\kappa_{\text{off,B}} C_{1,B} + 2\alpha_1 C_{1,B} - 2\kappa_{\text{on,B}} C_{1,B} r + 2\kappa_{\text{off,B}} C_{2,B} + 2\alpha_2 C_{2,B} \\
\frac{dC_{1,A}}{dt} &= \kappa_{\text{on,A}} R_A r - \kappa_{\text{off,A}} C_{1,A} - \alpha_1 C_{1,A} - \beta_1 \gamma_r C_{1,A} - \kappa_{\text{on,A}} C_{1,A} r + \kappa_{\text{off,A}} C_{2,A} + \beta_2 \gamma_r C_{2,A} \\
\frac{dC_{1,B}}{dt} &= \kappa_{\text{on,B}} R_B r - \kappa_{\text{off,B}} C_{1,B} - \alpha_1 C_{1,B} - \beta_1 \gamma_r C_{1,B} - \kappa_{\text{on,B}} C_{1,B} r + \kappa_{\text{off,B}} C_{2,B} + \beta_2 \gamma_r C_{2,B} \\
\frac{dC_{2,A}}{dt} &= 2\kappa_{\text{on,A}} C_{1,A} r - 2\kappa_{\text{off,A}} C_{2,A} - \alpha_2 C_{2,A} - 2\beta_2 \gamma_r C_{2,A} \\
\frac{dC_{2,B}}{dt} &= 2\kappa_{\text{on,B}} C_{1,B} r - 2\kappa_{\text{off,B}} C_{2,B} - \alpha_2 C_{2,B} - 2\beta_2 \gamma_r C_{2,B}
\end{aligned}$$

$$\begin{aligned}
\frac{dC_A}{dt} &= \kappa_{\text{on,Ribo}} R_A \text{Ribo} - \kappa_{\text{off,Ribo}} C_A \\
\frac{dC_B}{dt} &= \kappa_{\text{on,Ribo}} R_B \text{Ribo} - \kappa_{\text{off,Ribo}} C_B \\
\frac{d\text{Ribo}}{dt} &= -\kappa_{\text{on,Ribo}} (R_A + R_B) \text{Ribo} + \kappa_{\text{off,Ribo}} (C_A + C_B)
\end{aligned} \tag{5.1}$$

The species and rates are labeled as described in Sections 3.2 and 4.2.

As seen in Section 4.2, the total quantity of ribosomes, denoted as $Ribo_{tot}$, remains constant:

$$Ribo_{tot} = Ribo + C_A + C_B = \text{constant} \tag{5.2}$$

5.2 Simulations and Results

For the simulations, we used the two sets of parameters from the Chapter 4, along with the same initial conditions. The initial conditions and the parameter sets are summarized below.

Initial Conditions:

- $R(0) = 3$
- $r(0) = 0.75$
- $C_1(0) = 0$
- $C_2(0) = 0$
- $C_0(0) = 0$

Common Parameters:

- $\sigma_R = 3.58$
- $\gamma_R = 1$
- $\sigma_r = 2$
- $\gamma_r = 0.25$
- $\alpha_1 = 1$
- $\beta_1 = 1$
- $\alpha_2 = 12$
- $\beta_2 = 7$

Parameter	Set 1 (Biologically Plausible)	Set 2 (Biologically Implausible)
$\kappa_{\text{on,A}}$	10000	200
$\kappa_{\text{off,A}}$	7.7	0.1
$\kappa_{\text{on,B}}$	10000	300
$\kappa_{\text{off,B}}$	7.7	0.1
$\kappa_{\text{on,Ribo}}$	15000	1000
$\kappa_{\text{off,Ribo}}$	7.7	1

Table 5.1: Values of the different scaled parameters of the two sets.

In this model, compared to the previous one, given that we have a single miRNA that binds to both mRNAs, it was necessary to double the value of the miRNA synthesis rate, $\sigma_r = 2$, in order to obtain sustained oscillations. Following this adjustment, we varied σ_r in the simulations to observe how the system behaved under different conditions.

We then simulated the system using Set 2, the biologically implausible parameter set, and observed different behaviors compared to those in Chapter 4. Specifically, we noticed that for $\sigma_r = 1.8$ and $\sigma_r = 1.9$, the dynamics of C_A and C_B could not be unequivocally classified as in-phase or anti-phase, whereas this distinction was clearer for $\sigma_r = 1.7$ and $\sigma_r = 2.0$.

The consistency in in-phase or anti-phase dynamics for $\sigma_r = 1.7$ and $\sigma_r = 2.0$, irrespective of the variation in the ribosome pool concentration, highlights the impact of miRNA-mediated coupling. The shared miRNA exerts a competitive effect, providing a strong coupling mechanism between C_A and C_B, despite ribosome availability. This robustness points to a more rigid regulatory link compared to the behavior observed in Chapter 4, where separate miRNAs resulted in greater sensitivity to ribosome pool changes and less stable phase relationships.

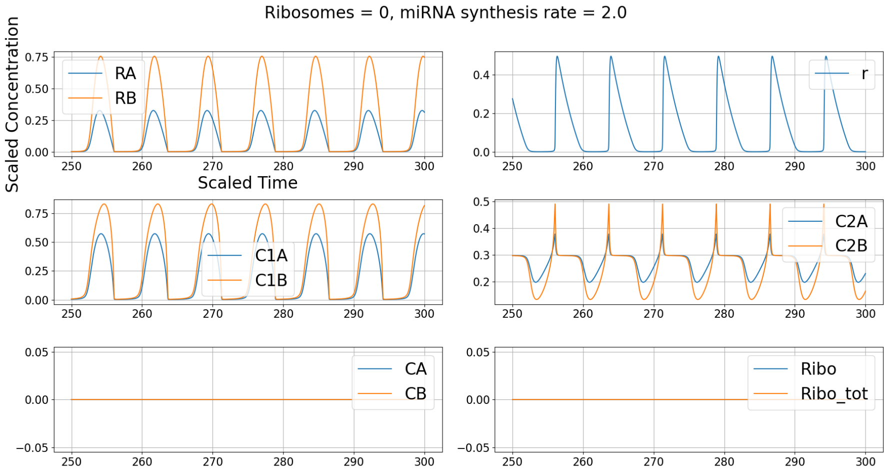

Figure 5.1: Dynamics of molecular species A and B with no initial ribosome pool ($Ribo(0) = Ribo_{tot} = 0$) for Set 1 parameters. The plots were obtained through numerical integration of the ODEs in Python, covering 0 to 300 time units, and focusing on the time range from 250 to 300 to highlight oscillatory behavior. Unlike what was observed in Chapter 4, miRNA sharing here couples all chemical species, effectively eliminating differences in period and phase.

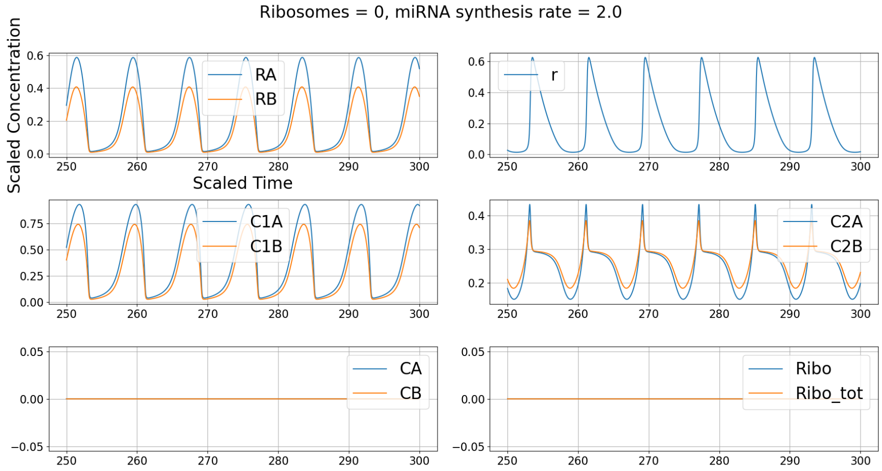

Figure 5.2: Dynamics of molecular species A and B with no initial ribosome pool ($Ribo(0) = Ribo_{tot} = 0$) for Set 2 parameters. The numerical integration method and time range are the same as in Figure 5.1. Unlike what was observed in Chapter 4, miRNA sharing here couples all chemical species, effectively eliminating differences in period and phase.

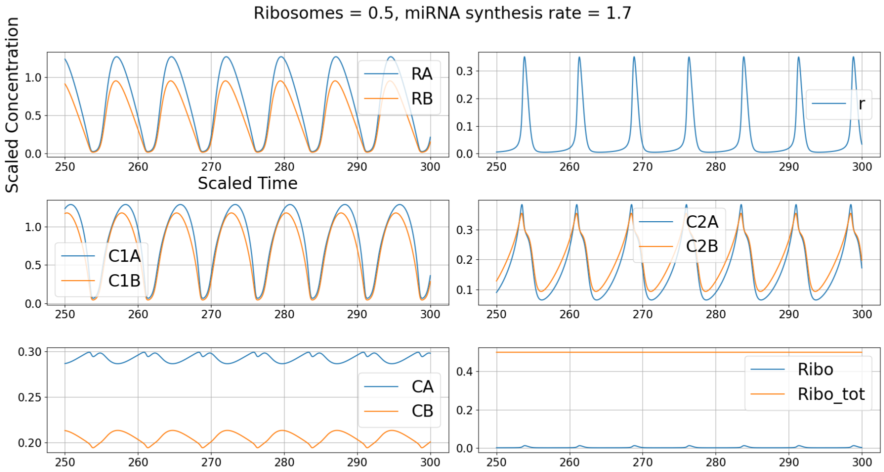

Figure 5.3: Dynamics of molecular species A and B for Set 2 parameters with $\sigma_r = 1.7$ and a limited ribosome pool ($Ribo(0) = Ribo_{tot} = 0.5$), showing anti-phase behavior between C_A and C_B. The plots were generated using numerical integration, similar to Figure 5.1.

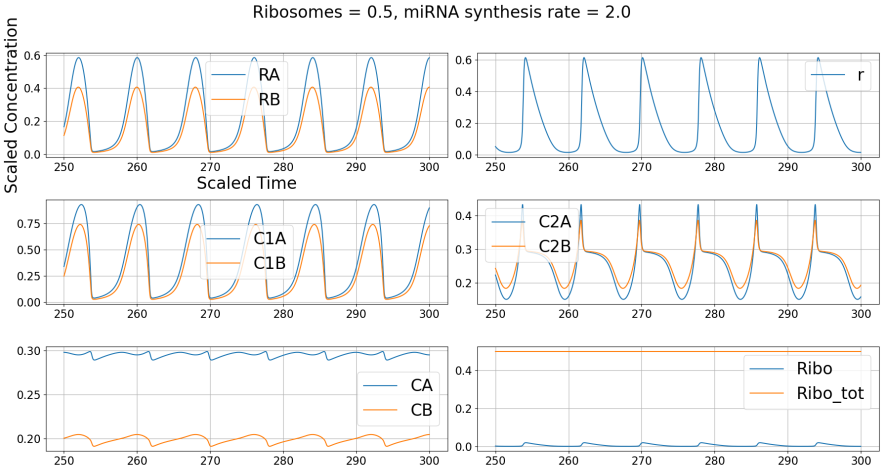

Figure 5.4: Dynamics of molecular species A and B for Set 2 parameters with $\sigma_r = 2.0$ and $Ribo(0) = Ribo_{tot} = 0.5$), showing in-phase behavior between C_A and C_B despite the presence of a limited pool of ribosomes. The integration method is consistent with that used in Figure 5.1.

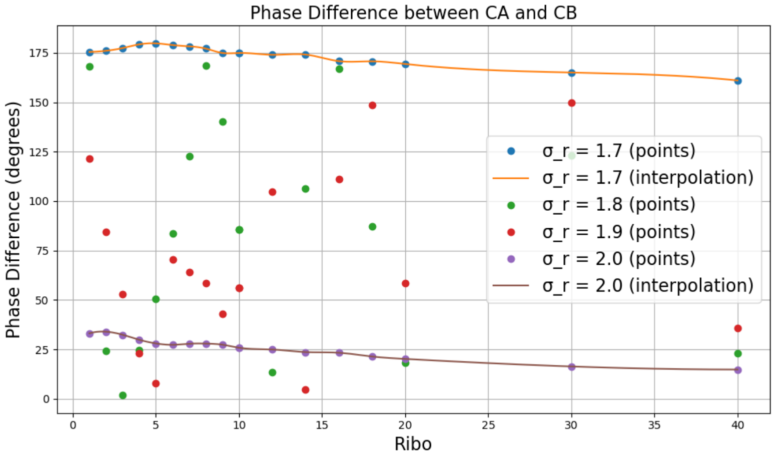

Figure 5.5: Phase difference between C_A and C_B as a function of ribosome pool concentration for different values of σ_r. Points represent simulation data, while lines show interpolated trends for $\sigma_r = 1.7$ and $\sigma_r = 2.0$. Green and red dots correspond to $\sigma_r = 1.8$ and $\sigma_r = 1.9$, respectively. Integration was performed from 0 to 300 time units, with phase differences calculated in the last 50 time units.

We also attempted to simulate the system for Set 1 of parameters, the biologically plausible set. However, for this set, the identification of in-phase and anti-phase dynamics remained ambiguous due to the signal shapes as one can see in Figures 5.6, 5.7, 5.8, 5.9.

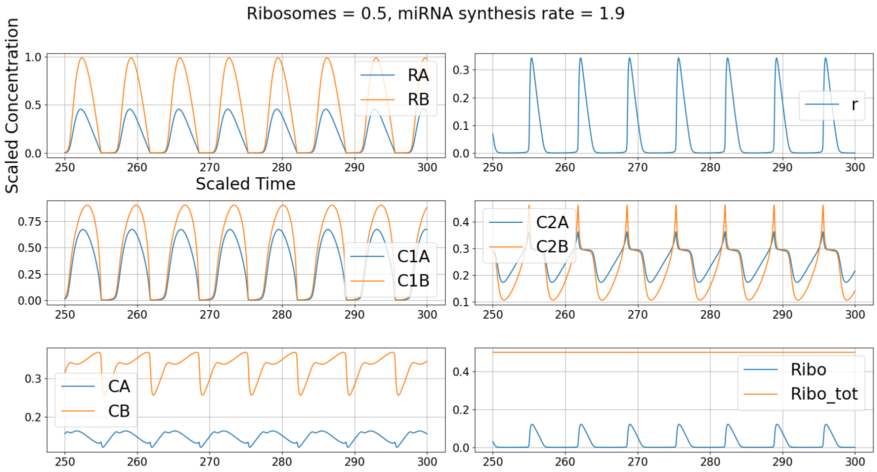

Figure 5.6: Dynamics of the system for Set 1 parameters with $\sigma_r = 1.9$ and a limited ribosome pool ($Ribo(0) = Ribo_{tot} = 0.5$). The signal shapes make it challenging to determine whether the dynamics are in-phase or anti-phase. Numerical integration was conducted as in Figure 5.1.

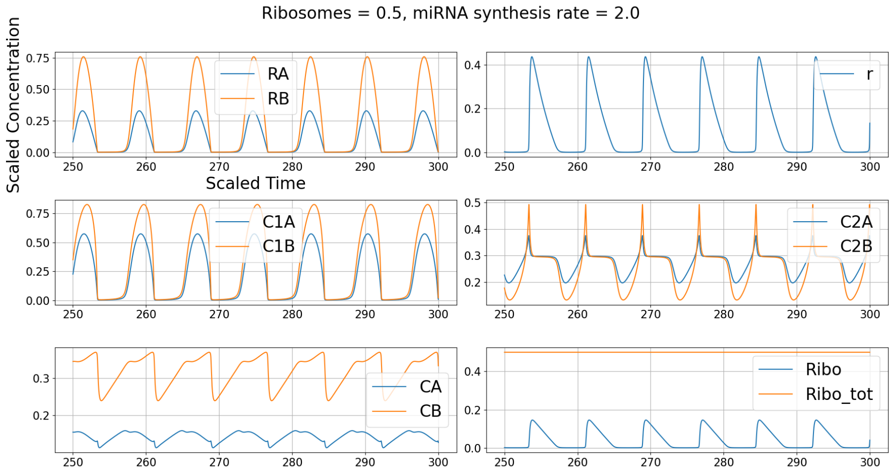

Figure 5.7: Dynamics of the system for Set 1 parameters with $\sigma_r = 2.0$ and a limited ribosome pool ($Ribo(0) = Ribo_{tot} = 0.5$). The ambiguous signal shapes persist, making it difficult to determine the phase relationship. Numerical integration was performed similarly to Figure 5.1.

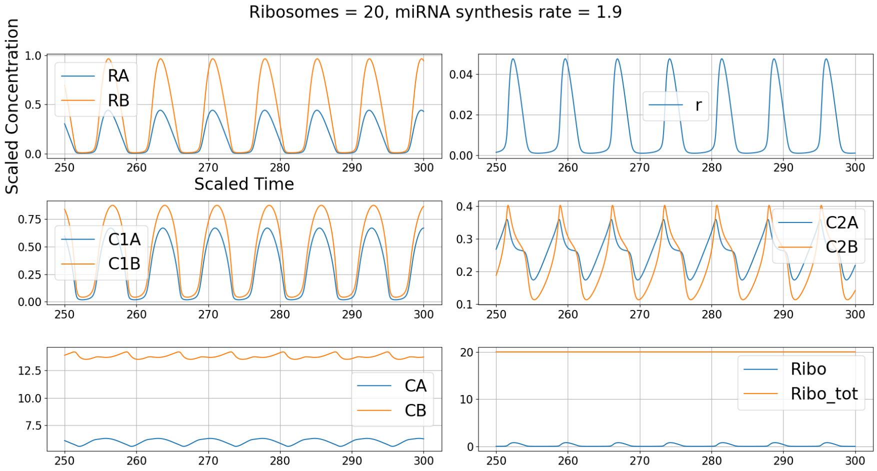

Figure 5.8: Dynamics of the system for Set 1 parameters with $\sigma_r = 1.9$ and an abundant ribosome pool ($Ribo(0) = Ribo_{tot} = 20$). The unclear phase relationships persist, complicating the determination of in-phase or anti-phase behavior. Integration was performed in the same manner as in Figure 5.1.

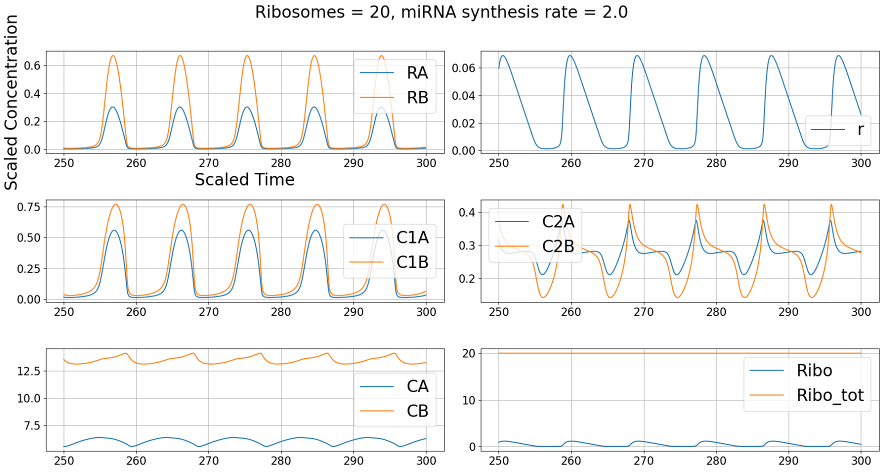

Figure 5.9: Dynamics of the system for Set 1 parameters with $\sigma_r = 2.0$ and an abundant ribosome pool ($Ribo(0) = Ribo_{tot} = 20$). As in previous cases, the complex oscillatory dynamics make it difficult to classify the phase relationship as either in-phase or anti-phase. The integration was conducted using the same approach as described in Figure 5.1.

5.3 Discussion

The analysis of the shared miRNA model reveals a more robust phase-locking behavior compared to the model presented in Chapter 4. The shared miRNA introduces a stronger coupling between C_A and C_B, resulting in consistent phase relationships that are less sensitive to variations in the ribosome pool. This is particularly evident in the biologically implausible parameter set, where either in-phase or anti-phase behavior was consistently maintained for specific values of σ_r, regardless of ribosome concentration.

In contrast, for the biologically plausible parameter set, the signals exhibited complex shapes that prevented a clear identification of the phase relationship. This suggests that, under more biologically realistic conditions, the system may operate in a regime where the miRNA-induced regulation results in more intricate dynamic behaviors that do not readily conform to simple in-phase or anti-phase classifications.

Chapter 6

Conclusions

This research began with the observation of time-sharing dynamics at both population and molecular levels. Liu et al. [1] demonstrated how bacterial biofilms, under nutrient-limiting conditions, achieve optimized growth through anti-phase oscillations in metabolic activities. Similarly, Park et al. [3] observed time-sharing in the competition for RNA polymerase within single bacterial cells. These studies identified the key ingredients of time-sharing: the presence of at least two oscillators coupled by a limiting shared resource.

Inspired by these findings, we extended the work of Nordick et al. [2], who identified sustained oscillations in mRNA, miRNA, and their complexes within a post-transcriptional circuit. To investigate time-sharing further, we expanded this model by introducing two types of mRNAs, each regulated by its respective miRNA, and coupled them through a shared ribosome pool. To observe time-sharing dynamics in the presence of a limited ribosome pool, we introduced differences in miRNA binding rates. This adjustment was necessary because molecular species of types A and B, with identical parameter sets, were unable to exhibit time-sharing dynamics—they effectively represented identical entities arbitrarily assigned different labels, even under conditions of resource competition.

Under limited ribosome availability, our models revealed anti-phase oscillations in mRNA-ribosome complexes (C_A and C_B) showcasing alternating access to the shared resource. This temporal separation reduced competition and enabled efficient resource utilization by both systems. When ribosome availability increased, the dynamics shifted to in-phase oscillations, reflecting simultaneous resource access. The asymmetry was necessary to create a dynamic hierarchy where the more repressed mRNA initially lagged in ribosome recruitment but later exploited dissociation phases of the dominant mRNA. This staggered binding enabled the more repressed mRNA to establish anti-phase oscillations as ribosomes became transiently available. These results underscore the critical role of resource constraints in driving time-sharing dynamics and demonstrate the potential for synchronization under abundant resources.

We also modeled a shared miRNA scenario, where both mRNA types were regulated by the same miRNA. This configuration, reflecting some real cellular conditions, introduced a strong coupling mechanism between C_A and C_B. The shared miRNA led to robust and consistent phase relationships, with either in-phase or anti-phase dynamics depending on the miRNA synthesis rate but not sensitive to ribosome availability. However, with biologically plausible parameters, the dynamics became complex and resisted simple phase classification, suggesting additional regulatory layers introduced by shared miRNA interactions.

Overall, our findings reveal that time-sharing dynamics are a generalizable principle for optimizing limited resources in biological systems. The interactions between mRNAs, miRNAs, and ribosomes illustrate how resource constraints and coupling mechanisms shape oscillatory behaviors. Robust anti-phase dynamics under constrained conditions align with principles observed in biofilms and molecular systems, while the transition to in-phase dynamics with abundant resources highlights the adaptability of biological networks.

Future work should incorporate stochastic elements to understand the role of noise in oscillatory reliability and validate the models experimentally to confirm theoretical predictions. This research provides a unified perspective on time-sharing across biological scales, advancing our understanding of how cells balance competition and cooperation to maintain homeostasis under resource-limited conditions.

Bibliography

[1] J. Liu, R. Martinez-Corral, A. Prindle, D.-Y. D. Lee, J. Larkin, M. Gabalda-Sagarra, J. Garcia Ojalvo, and G. M. Süel. «Coupling between distant biofilms and emergence of nutrient time-sharing». In: *Science* 356.6339 (2017), pp. 638–642. DOI: `10.1126/science.aal4082` (cit. on pp. ii, 1–4, 6, 30, 31, 58).

[2] B. Nordick, P. Y. Yu, G. Liao, and T. Hong. «Nonmodular oscillator and switch based on RNA decay drive regeneration of multimodal gene expression». In: *Nucleic Acids Research* 50.7 (2022), pp. 3693–3708. DOI: `10.1093/nar/gkac217` (cit. on pp. ii, 9, 14, 16, 17, 19, 21–23, 25, 29, 58).

[3] J. Park et al. «Molecular Time Sharing through Dynamic Pulsing in Single Cells». In: *Cell Systems* 6.2 (Feb. 2018), pp. 216–229. DOI: `10.1016/j.cels.2018.01.011` (cit. on pp. 1, 6, 7, 30, 31, 58).

[4] Bruce Alberts, Alexander Johnson, Julian Lewis, Martin Raff, Keith Roberts, and Peter Walter. *Molecular Biology of the Cell.* 7th. New York, NY: Garland Science, 2022. ISBN: 9780815344643 (cit. on p. 9).

[5] Fabian Afonso-Grunz and Sören Müller. «Principles of miRNA–mRNA interactions: beyond sequence complementarity». In: *Cellular and Molecular Life Sciences* 72 (2015), pp. 3127–3141. DOI: `10.1007/s00018-015-1922-2` (cit. on pp. 10, 11).

[6] Authors from Frontiers Journal. «MicroRNAs: From Mechanism to Organism». In: *Frontiers in Cell and Developmental Biology* (2020). URL: `https://www.frontiersin.org/journals/cell-and-developmental-biology/articles/10.3389/fcell.2020.00409/full` (cit. on p. 10).

[7] Hironori Matsuyama and Hiroshi I. Suzuki. «Systems and Synthetic microRNA Biology: From Biogenesis to Disease Pathogenesis». In: *International Journal of Molecular Sciences* 21.1 (2020), p. 132. DOI: `10.3390/ijms21010132` (cit. on p. 11).

[8] Venkatraman Ramakrishnan. «Ribosome Structure and Function: Insights from Recent Studies». In: *Annual Review of Biophysics* 49 (2020), pp. 283–304. DOI: `10.1146/annurev-biophys-121219-081653` (cit. on p. 11).

[9] Rémi Tanguy and Masayuki Mori. «Ribosomal Modifications and Their Role in Translational Control Under Stress». In: *Molecular Cell* 81 (2021), pp. 2126–2140. DOI: `10.1016/j.molcel.2021.03.018` (cit. on p. 11).

[10] Renana Sabi and Tamir Tuller. «Modelling and measuring intracellular competition for finite resources during gene expression». In: *Journal of The Royal Society Interface* 16.20180887 (2019), pp. 1–15. DOI: `10.1098/rsif.2018.0887` (cit. on p. 12).

[11] Alon Raveh, Michael Margaliot, Eduardo D. Sontag, and Tamir Tuller. «A Model for Competition for Ribosomes in the Cell». In: *ArXiv* (2015). eprint: `1508.02408v1`. URL: `http://arxiv.org/abs/1508.02408v1` (cit. on p. 12).

[12] Pascal S. Rogalla, Timothy J. Rudge, and Luca Ciandrini. «An equilibrium model for ribosome competition». In: *Physical Biology* 17 (2020), p. 015002. DOI: `10.1088/1478-3975/ab4fbc` (cit. on p. 12).

[13] Sofie Snoeck, Chiara Guidi, and Marjan De Mey. «Metabolic burden explained: stress symptoms and its related responses induced by (over)expression of (heterologous) proteins in Escherichia coli». In: *Microbial Cell Factories* 23 (2024), p. 96. DOI: `10.1186/s12934-024-02370-9` (cit. on p. 12).

[14] L.V. Sharova, A.A. Sharov, T. Nedorezov, Y. Piao, N. Shaik, and M.S.H. Ko. «Database for mRNA half-life of 19 977 genes obtained by DNA microarray analysis of pluripotent and differentiating mouse embryonic stem cells». In: *DNA Research* 16 (2009), pp. 45–58 (cit. on p. 21).

[15] L.Y. Chan, C.F. Mugler, S. Heinrich, P. Vallotton, and K. Weis. «Non-invasive measurement of mRNA decay reveals translation initiation as the major determinant of mRNA stability». In: *Elife* 7 (2018), e32536 (cit. on p. 21).

[16] E. Yang, E. van Nimwegen, M. Zavolan, N. Rajewsky, M. Schroeder, M. Magnasco, and J.E. Darnell. «Decay rates of human mRNAs: correlation with functional characteristics and sequence attributes». In: *Genome Research* 13 (2003), pp. 1863–1872 (cit. on p. 21).

[17] E. Zlotorynski. «Insights into the kinetics of microRNA biogenesis and turnover». In: *Nature Reviews Molecular Cell Biology* 20 (2019), pp. 511–511 (cit. on p. 21).

[18] B. Reichholf, V.A. Herzog, N. Fasching, R.A. Manzenreither, I. Sowemimo, and S.L. Ameres. «Time-resolved small RNA sequencing unravels the molecular principles of microRNA homeostasis». In: *Molecular Cell* 75 (2019), pp. 756–768 (cit. on p. 21).

[19] M.J. Moore, J.A. Sebastian, and M.C. Kolios. «Determination of cell nucleus-to-cytoplasmic ratio using imaging flow cytometry and a combined ultrasound and photoacoustic technique: a comparison study». In: *Journal of Biomedical Optics* 24 (2019), p. 106502 (cit. on p. 21).

[20] J. Gingras, R.M. Rioux, D. Cuvelier, N.A. Geisse, J.W. Lichtman, G.M. Whitesides, L. Mahadevan, and J.R. Sanes. «Controlling the orientation and synaptic differentiation of myotubes with micropatterned substrates». In: *Biophysical Journal* 97 (2009), pp. 2771–2779 (cit. on p. 21).

[21] A. Bartholomäus et al. «Bacteria differently regulate mRNA abundance to specifically respond to various stresses». In: *Philosophical Transactions of the Royal Society A: Mathematical, Physical and Engineering Sciences* 374.2063 (2016). p. 4, 3rd paragraph, p. 20150069. DOI: `10.1098/rsta.2015.0069` (cit. on p. 21).

[22] T. von der Haar. «A quantitative estimation of the global translational activity in logarithmically growing yeast cells». In: *BMC Systems Biology* 2 (2008). p. 8 of 14, right column, 2nd paragraph, p. 87. DOI: `10.1186/1752-0509-2-87` (cit. on p. 21).

[23] F. Tang, K. Lao, and M. A. Surani. «Development and applications of single-cell transcriptome analysis». In: *Nature Methods* 8.4 Suppl (2011). p. 3 bottom paragraph, S6–S11. DOI: `10.1038/nmeth.1557` (cit. on p. 22).

[24] N. Pinzón, B. Li, L. Martinez, A. Sergeeva, J. Presumey, F. Apparailly, and H. Seitz. «microRNA target prediction programs predict many false positives». In: *Genome Research* 27 (2017), pp. 234–245 (cit. on p. 22).

[25] L.M. Wee, C.F. Flores-Jasso, W.E. Salomon, and P.D. Zamore. «Argonaute divides its RNA guide into domains with distinct functions and RNA-binding properties». In: *Cell* 151 (2012), pp. 1055–1067 (cit. on p. 22).

[26] S.H. Koenig and R.D. Brown. «H2CO3 as substrate for carbonic anhydrase in the dehydration of HCO3». In: *Proceedings of the National Academy of Sciences of the USA* 69 (1972), pp. 2422–2425 (cit. on p. 23).

[27] G.Q. Zhou and W.Z. Zhong. «Diffusion-Controlled Reactions of Enzymes: A Comparison between Chou's Model and Alberty-Hammes-Eigen's Model». In: *European Journal of Biochemistry* 128 (1982), pp. 383–387 (cit. on p. 23).

[28] S. W. Eichhorn et al. «mRNA destabilization is the dominant effect of mammalian microRNAs by the time substantial repression ensues». In: *Molecular Cell* 56 (2014), pp. 104–115 (cit. on pp. 23, 24).

[29] M. de la Mata, D. Gaidatzis, M. Vitanescu, M. B. Stadler, C. Wentzel, P. Scheiffele, W. Filipowicz, and H. Gro. «Potent degradation of neuronal miRNAs induced by highly complementary targets». In: *EMBO Reports* 16 (2015), pp. 500–511 (cit. on pp. 23, 24).

[30] A. Baccarini, H. Chauhan, T. J. Gardner, A. D. Jayaprakash, R. Sachidanandam, and B. D. Brown. «Kinetic analysis reveals the fate of a microRNA following target regulation in mammalian cells». In: *Current Biology* 21 (2011), pp. 369–376 (cit. on pp. 23, 24).

[31] F. Ghini, C. Rubolino, M. Climent, I. Simeone, M. J. Marzi, and F. Nicassio. «Endogenous transcripts control miRNA levels and activity in mammalian cells by target-directed miRNA degradation». In: *Nature Communications* 9 (2018), p. 3119 (cit. on pp. 23, 24).

[32] R. A. Freitas Jr. and R. C. Merkle. *Kinematic Self-Replicating Machines.* Link - link 2nd paragraph. Georgetown, TX: Landes Bioscience, 2004 (cit. on p. 33).

[33] R. Milo and R. Phillips. *Cell Biology by the Numbers.* Garland Science, 2015 (cit. on p. 33).

[34] P. Shah, Y. Ding, M. Niemczyk, G. Kudla, and J. B. Plotkin. «Rate-limiting steps in yeast protein translation». In: *Cell* 153.7 (2013), pp. 1589–1601 (cit. on p. 33).

[35] A. Valleriani, Z. Ignatova, A. Nagar, and R. Lipowsky. «Turnover of messenger RNA: Polysome statistics beyond the steady state». In: *EPL (Europhysics Letters)* 89.5 (2010). p.58003-p3 left column 3rd paragraph, p. 58003. DOI: `10.1209/0295-5075/89/58003` (cit. on p. 33).

[36] Luis Mier-y-Terán-Romero, Mary Silber, and Vassily Hatzimanikatis. «The Origins of Time-Delay in Template Biopolymerization Processes». In: *PLoS Computational Biology* 6.4 (2010), e1000726. DOI: `10.1371/journal.pcbi.1000726` (cit. on p. 48).

[37] Manuel Barrio, Kevin Burrage, Andre Leier, and Tianhai Tian. «Oscillatory Regulation of Hes1: Discrete Stochastic Delay Modelling and Simulation». In: *PLoS Computational Biology* 2.9 (2006), e117. DOI: `10.1371/journal.pcbi.0020117` (cit. on p. 48).

[38] Valerio Licursi, Federica Conte, Giulia Fiscon, and Paola Paci. «MIENTURNET: An interactive web tool for microRNA-target enrichment and network-based analysis». In: *BMC Bioinformatics* 20.1 (2019), p. 545. DOI: `10.1186/s12859-019-3105-x` (cit. on p. 50).